

Figure 6 (see previous page)

Various tumors that developed spontaneously in *p53* medaka knockouts. (a,b) The tumor that arose in the left gill of a *p53*^{E241X/+} fish with the lymphomatous infiltrate, consistent with the diagnosis of thymic lymphoma. (c,d) Adenocarcinoma found in the right gill of a *p53*^{E241X/E241X} homozygous fish. (e,f) Retinoblastoma in the right eye of a *p53*^{E241X/E241X} homozygous fish. Note the rosette-like structures throughout the tumor. (g,h) A germ cell tumor found in the anterior upper part of the peritoneal cavity of a *p53*^{E241X/E241X} homozygous fish. All fish presented here died or were sacrificed at around 8 months of age. Arrowheads indicate tumors. Hematoxylin-eosin staining, original magnification: (b,d) 100×; (f,h) 10×.

were obtained that developed to adulthood. Progeny were genotyped by sequencing and heterozygous fish carrying the mutation of interest were incrossed to obtain homozygous fish.

***p53* target gene induction**

For most of the studies, the *p53*^{E241X} allele was used. F2 *p53*^{+/^{E241X} heterozygous fish resulting from the *in vitro* fertilization were incrossed to produce F3 progeny of all genotypes. Four days post-fertilization, F3 embryos were irradiated with 20 Gy of ionizing radiation using ¹³⁷Cs (0.02 Gy/s, Gammacell 40, Atomic Energy of Canada Limited Industrial Products, Ontario). Six hours later, the embryos were frozen in liquid nitrogen and RNA was extracted by Trizol (Invitrogen, Carlsbad, CA, USA) according to the manufacturer's instruction. The embryos were genotyped by PCR and resequencing of the simultaneously extracted genomic DNA. cDNA was synthesized from each genotype using SuperScript III (Invitrogen). The mRNA expression levels were determined by PCR reactions (94°C for 1 minute; predetermined cycles of 94°C for 30 s, 55°C for 20 s, 72°C for 30 s). The numbers of cycles used were: *β-actin*, 15; *Mdm2*, 24; and *p53*, *p21* and *Bax*, 26. Details on oligonucleotides used can be obtained from the authors upon request.}

Apoptosis assay

Primary cell cultures derived from *p53*^{E241X/E241X} and *p53*^{+/⁺ embryos were obtained as described previously [42]. Cells (1.5 × 10⁵) were inoculated in a 35 mm dish and irradiated with 10 Gy of γ -rays. The cells were monitored for fragmentation using a IX81 inverted microscope (Olympus, Tokyo, Japan) controlled by IPLab software (BD Biosciences, Rockville, MD, USA) from zero to eight hours after γ -irradiation.}

Histology

After tumors were observed under the stereomicroscope, fish were fixed in 4% paraformaldehyde for 24 hours and embedded in paraffin. Tissue sections were stained by standard hematoxylin-eosin staining. Photographs of the slides were obtained by a VC4500G digital camera (Omron, Kyoto, Japan) mounted on an ECLIPSE E800 microscope (Nikon, Tokyo, Japan).

Acknowledgements

We thank R Ohta, R Hamaguchi, Y Yoshiura, S Yonezawa, H Miyamoto, N Matsuo and all technical staff of Sequencing Technology Team RIKEN GSC for technical assistance. We thank the medaka genome sequencing consortium for sharing sequence information prior to publication. This work was supported by grants-in-aid from the Ministry of Education, Sports and Culture of Japan and an investment grant from the Netherlands Organization for Scientific Research (NWO) to RHAP and EC.

References

1. Wittbrodt J, Shima A, Scharf M: **Medaka - a model organism from the far East.** *Nat Rev Genet* 2002, **3**:53-64.
2. Hawkins WE, Walker WW, Fournie JW, Manning CS, Krol RM: **Use of the Japanese medaka (*Oryzias latipes*) and guppy (*Poecilia reticulata*) in carcinogenesis testing under national toxicology program protocols.** *Toxicol Pathol* 2003, **31**(Suppl):88-91.
3. Driever W, Solnica-Krezel L, Schier AF, Neuhaus SC, Malicki J, Stemple DL, Stainier DY, Zwartkruis F, Abdellah S, Rangini Z, et al.: **A genetic screen for mutations affecting embryogenesis in zebrafish.** *Development* 1996, **123**:37-46.
4. Furutani-Seiki M, Sasado T, Morinaga C, Suwa H, Niwa K, Yoda H, Deguchi T, Hirose Y, Yasuoka A, Henrich T, et al.: **A systematic genome-wide screen for mutations affecting organogenesis in Medaka, *Oryzias latipes*.** *Mech Dev* 2004, **121**:647-658.
5. Haffter P, Granato M, Brand M, Mullins MC, Hammerschmidt M, Kane DA, Odenthal J, van Eeden FJ, Jiang YJ, Heisenberg CP, et al.: **The identification of genes with unique and essential functions in the development of the zebrafish, *Danio rerio*.** *Development* 1996, **123**:1-36.
6. Tautz D: **Redundancies, development and the flow of information.** *Bioessays* 1992, **14**:263-266.
7. Jaillon O, Aury JM, Brunet F, Petit JL, Stange-Thomann N, Mauceli E, Bouneau L, Fischer C, Ozouf-Costaz C, Bernot A, et al.: **Genome duplication in the teleost fish *Tetraodon nigroviridis* reveals the early vertebrate proto-karyotype.** *Nature* 2004, **431**:946-957.
8. **Medaka Genome Project** [http://dolphin.lab.nig.ac.jp/medaka]
9. Nasevicius A, Ekker SC: **Effective targeted gene 'knockdown' in zebrafish.** *Nat Genet* 2000, **26**:216-220.
10. Fan L, Moon J, Crodian J, Collodi P: **Homologous recombination in zebrafish ES cells.** *Transgenic Res* 2006, **15**:21-30.
11. Wienholds E, Schulte-Merker S, Walderich B, Plasterk RH: **Target-selected inactivation of the zebrafish *rag1* gene.** *Science* 2002, **297**:99-102.
12. Wienholds E, van Eeden F, Kusters M, Mudde J, Plasterk RH, Cuppen E: **Efficient target-selected mutagenesis in zebrafish.** *Genome Res* 2003, **13**:2700-2707.
13. Li Q, Liu Z, Monroe H, Cui CT: **Integrated platform for detection of DNA sequence variants using capillary array electrophoresis.** *Electrophoresis* 2002, **23**:1499-1511.
14. McCallum CM, Comai L, Greene EA, Henikoff S: **Targeted screening for induced mutations.** *Nat Biotechnol* 2000, **18**:455-457.
15. Smits BM, Mudde JB, van de Belt J, Verheul M, Olivier J, Homberg J, Gurjev V, Cools AR, Ellenbroek BA, Plasterk RH, Cuppen E: **Generation of gene knockouts and mutant models in the laboratory rat by ENU-driven target-selected mutagenesis.** *Pharmacogenet Genomics* 2006, **16**:159-169.
16. Stephens M, Sloan JS, Robertson PD, Scheet P, Nickerson DA: **Automating sequence-based detection and genotyping of SNPs from diploid samples.** *Nat Genet* 2006, **38**:375-381.
17. Chen S, Hong Y, Scherer SJ, Scharf M: **Lack of ultraviolet-light inducibility of the medakafish (*Oryzias latipes*) tumor suppressor gene *p53*.** *Gene* 2001, **264**:197-203.

18. Yu J, Zhang L, Hwang PM, Rago C, Kinzler KW, Vogelstein B: Identification and classification of p53-regulated genes. *Proc Natl Acad Sci USA* 1999, 96:14517-14522.
19. Maquat LE: Nonsense-mediated mRNA decay: splicing, translation and mRNP dynamics. *Nat Rev Mol Cell Biol* 2004, 5:89-99.
20. Amatruda JF, Zon LI: Dissecting hematopoiesis and disease using the zebrafish. *Dev Biol* 1999, 216:1-15.
21. Masahito P, Aoki K, Egami N, Ishikawa T, Sugano H: Life-span studies on spontaneous tumor development in the medaka (*Oryzias latipes*). *Jpn J Cancer Res* 1989, 80:1058-1065.
22. Berghmans S, Murphey RD, Wienholds E, Neubergh D, Kutok JL, Fletcher CD, Morris JP, Liu TX, Schulte-Merker S, Kanki JP, et al: tp53 mutant zebrafish develop malignant peripheral nerve sheath tumors. *Proc Natl Acad Sci USA* 2005, 102:407-412.
23. Donehower LA, Harvey M, Slagle BL, McArthur MJ, Montgomery CA Jr, Butel JS, Bradley A: Mice deficient for p53 are developmentally normal but susceptible to spontaneous tumours. *Nature* 1992, 356:215-221.
24. Li FP, Fraumeni JF Jr, Mulvihill JJ, Blattner WA, Dreyfus MG, Tucker MA, Miller RW: A cancer family syndrome in twenty-four kindreds. *Cancer Res* 1988, 48:5358-5362.
25. Giasson BI, Lee VM: Parkin and the molecular pathways of Parkinson's disease. *Neuron* 2001, 31:885-888.
26. Hattori N, Matsumine H, Asakawa S, Kitada T, Yoshino H, Elibol B, Brookes AJ, Yamamura Y, Kobayashi T, Wang M, et al: Point mutations (Thr240Arg and Gln311Stop) [correction of Thr240Arg and Ala311Stop] in the Parkin gene. *Biochem Biophys Res Commun* 1998, 249:754-758.
27. Ellis NA, Groden J, Ye TZ, Straughen J, Lennon DJ, Ciocchi S, Proytcheva M, German J: The Bloom's syndrome gene product is homologous to RecQ helicases. *Cell* 1995, 83:655-666.
28. Chester N, Kuo F, Kozak C, O'Hara CD, Leder P: Stage-specific apoptosis, developmental delay, and embryonic lethality in mice homozygous for a targeted disruption in the murine Bloom's syndrome gene. *Genes Dev* 1998, 12:3382-3393.
29. Furutani-Seiki M, Wittbrodt J: Medaka and zebrafish, an evolutionary twin study. *Mech Dev* 2004, 121:629-637.
30. Hyodo-Taguchi Y: Inbred strains of the medaka (*Oryzias latipes*). *Fish Biol J Medaka* 1996, 8:29-30.
31. Cho Y, Gorina S, Jeffrey PD, Pavletich NP: Crystal structure of a p53 tumor suppressor-DNA complex: understanding tumorigenic mutations. *Science* 1994, 265:346-355.
32. Joerger AC, Allen MD, Fersht AR: Crystal structure of a superstable mutant of human p53 core domain. Insights into the mechanism of rescuing oncogenic mutations. *J Biol Chem* 2004, 279:1291-1296.
33. Rolley N, Butcher S, Milner J: Specific DNA binding by different classes of human p53 mutants. *Oncogene* 1995, 11:763-770.
34. Dimitrijevic N, Winkler C, Wellbrock C, Gomez A, Duschl J, Altschmid J, Scharl M: Activation of the Xmrk proto-oncogene of Xiphophorus by overexpression and mutational alterations. *Oncogene* 1998, 16:1681-1690.
35. Langenau DM, Traver D, Ferrando AA, Kutok JL, Aster JC, Kanki JP, Lin S, Prochowick E, Trede NS, Zon LI, Look AT: Myc-induced T cell leukemia in transgenic zebrafish. *Science* 2003, 299:887-890.
36. Haramis AP, Hurlstone A, van der Velden Y, Begthel H, van den Born M, Offerhaus GJ, Clevers HC: Adenomatous polyposis coli-deficient zebrafish are susceptible to digestive tract neoplasia. *EMBO Rep* 2006, 7:444-449.
37. Krause MK, Rhodes LD, Van Beneden RJ: Cloning of the p53 tumor suppressor gene from the Japanese medaka (*Oryzias latipes*) and evaluation of mutational hotspots in MNNG-exposed fish. *Gene* 1997, 189:101-106.
38. Patton EE, Widelund HR, Kutok JL, Kopani KR, Amatruda JF, Murphey RD, Berghmans S, Mayhall EA, Traver D, Fletcher CD, et al: BRAF mutations are sufficient to promote nevi formation and cooperate with p53 in the genesis of melanoma. *Curr Biol* 2005, 15:249-254.
39. Medaka Book 3.3.1 Cryo-preservation of Medaka sperm [<http://www.shigen.nig.ac.jp/medaka/medakabook/index.php?3.3.1%20Cryo-preservation%20of%20Medaka%20sperm>]
40. LIMSTILL: Laboratory Information System for the Identification of Mutations by sequencing and TILLing [<http://limstill.niob.knaw.nl>]
41. Nickerson DA, Tobe VO, Taylor SL: PolyPhred: automating the detection and genotyping of single nucleotide substitutions using fluorescence-based resequencing. *Nucleic Acids Res* 1997, 25:2745-2751.
42. Komura J, Mitani H, Shima A: Fish cell culture: Establishment of two fibroblast-like cell lines (OL-17 and OL-32) from fin of the Medaka, *Oryzias latipes*. *In Vitro Cell Dev Biol* 1998, 24:294-298.

Electron Nuclear Double Resonance Differentiates Complementary Roles for Active Site Histidines in (6-4) Photolyase*

Received for publication, May 17, 2006, and in revised form, December 8, 2006. Published, JBC Papers in Press, December 12, 2006, DOI 10.1074/jbc.M604734200

Erik Schleicher[‡], Kenichi Hitomi^{§1}, Christopher W. M. Kay^{¶¶}, Elizabeth D. Getzoff[§], Takeshi Todo^{||}, and Stefan Weber^{‡2}

From the [‡]Fachbereich Physik, Freie Universität Berlin, Arnimallee 14, 14195 Berlin, Germany, the [§]Department of Molecular Biology and the Skaggs Institute for Chemical Biology, The Scripps Research Institute, La Jolla, California 92037, the [¶]Department of Biology, University College London, Gower Street, London WC1E 6BT, United Kingdom, and the ^{||}Radiation Biology Center, Kyoto University, Yoshidakonoe-cho, Sakyo-ku, Kyoto 606-8501, Japan

(6-4) photolyase catalyzes the light-dependent repair of UV-damaged DNA containing (6-4) photoproducts. Blue light excitation of the enzyme generates the neutral FAD radical, FADH[•], which is believed to be transiently formed during the enzymatic DNA repair. Here (6-4) photolyase has been examined by optical spectroscopy, electron paramagnetic resonance, and pulsed electron nuclear double resonance spectroscopy. Characterization of selected proton hyperfine couplings of FADH[•], namely those of H^{8α} and H¹, yields information on the micropolarity at the site where the DNA substrate is expected to bind. Shifts in the hyperfine couplings as a function of structural modifications induced by point mutations and pH changes distinguish the protonation states of two highly conserved histidines, His³⁵⁴ and His³⁵⁸, in *Xenopus laevis* (6-4) photolyase. These are proposed to catalyze formation of the oxetane intermediate that precedes light-initiated DNA repair. The results show that at pH 9.5, where the enzymatic repair activity is highest, His³⁵⁸ is deprotonated, whereas His³⁵⁴ is protonated. Hence, the latter is likely the proton donor that initiates oxetane formation from the (6-4) photoproduct.

Ultraviolet light ($\lambda \leq 300$ nm) damages cellular DNA by the formation of cyclobutane pyrimidine dimers (CPDs)³ and (6-4) photoproducts from adjacent pyrimidine bases on the same DNA strand (1). Such dimers are restored to their monomeric form by the action of two photoactive (300 < λ < 500 nm) damage-specific DNA repair enzymes, named CPD photolyase and (6-4) photolyase, collectively known as DNA photolyases (2–6). Both enzymes are found in various organisms, exhibit a

20–30% amino acid sequence identity (2, 7, 8), and share a common chromophore, FAD (9–12), although the two photolyases differ in DNA substrate specificity and repair mechanism.

For the CPD photolyase, the initial step in the proposed repair mechanism (13) is a photoinduced electron transfer from the fully reduced FAD cofactor (FADH[•]) to the CPD, resulting in the formation of a CPD anion radical and a neutral FADH[•] radical. The cyclobutane ring of the unstable CPD radical opens, and subsequently the electron is transferred back to the FADH[•] radical, thus restoring the initial redox states of both the FAD and the pair of pyrimidine bases in the DNA. Thus the entire process represents a true catalytic cycle with net-zero exchanged electrons.

Unlike CPD photolyase, (6-4) photolyases are not able to directly restore the original bases from the (6-4) photoproduct in UV-damaged DNA; rather, following binding of the lesion, the overall repair reaction consists of two distinct steps, one of which is light-independent and the other one light-dependent (Fig. 1) (14–16). In the initial light-independent step, a 6'-iminium ion is thought to be generated via proton transfer induced by two histidines highly conserved among the (6-4) photolyases (His³⁵⁴ and His³⁵⁸ in *Xenopus laevis* (6-4) photolyase) (16) (Fig. 2). This intermediate spontaneously rearranges to form an oxetane intermediate by intramolecular nucleophilic attack. Such a mechanism requires that one histidine acts as a proton acceptor and the other as a proton donor (see Fig. 2), which implies that the two histidines should have markedly different pK_a values. However, until now it has not been established which histidine acts as an acid and which one functions as a base. The proposed reaction mechanism is based on a biochemical study using alanine-substituted mutants (16), and as yet spectroscopy has not been employed to address this stage of the reaction.

In the subsequent light-driven reaction, one electron is believed to be transferred from the fully reduced FAD cofactor (FADH[•]) to the oxetane intermediate thus forming a neutral FADH[•] radical and an anionic oxetane radical, which spontaneously fractures. The excess electron is then back-transferred to the flavin radical restoring the fully reduced flavin cofactor and a pair of pyrimidine bases (see Fig. 1).

When the FAD cofactor is not in its catalytically active (fully reduced) redox state, another photoreaction takes place both in

* This work was supported by VolkswagenStiftung Grant I/77100 (to S. W.), Deutsche Forschungsgemeinschaft Sfb-498, Project A2 (to S. W.), and in part National Institutes of Health by Grant-in-aid R01 GM37684 (to E. D. G.). The costs of publication of this article were defrayed in part by the payment of page charges. This article must therefore be hereby marked "advertisement" in accordance with 18 U.S.C. Section 1734 solely to indicate this fact.

¹ Present address: Division of Chemistry, Graduate School of Engineering Science, Osaka University, 1-3 Machikaneyama, Toyonaka, Osaka 560-8531, Japan.

² To whom correspondence should be addressed. Tel.: 49-30-838-56139; Fax: 49-30-838-56046; E-mail: Stefan.Weber@physik.fu-berlin.de.

³ The abbreviations used are: CPD, cyclobutane pyrimidine dimer; ENDOR, electron nuclear double resonance; mT, millitesla.

ENDOR on (6-4) Photolyase

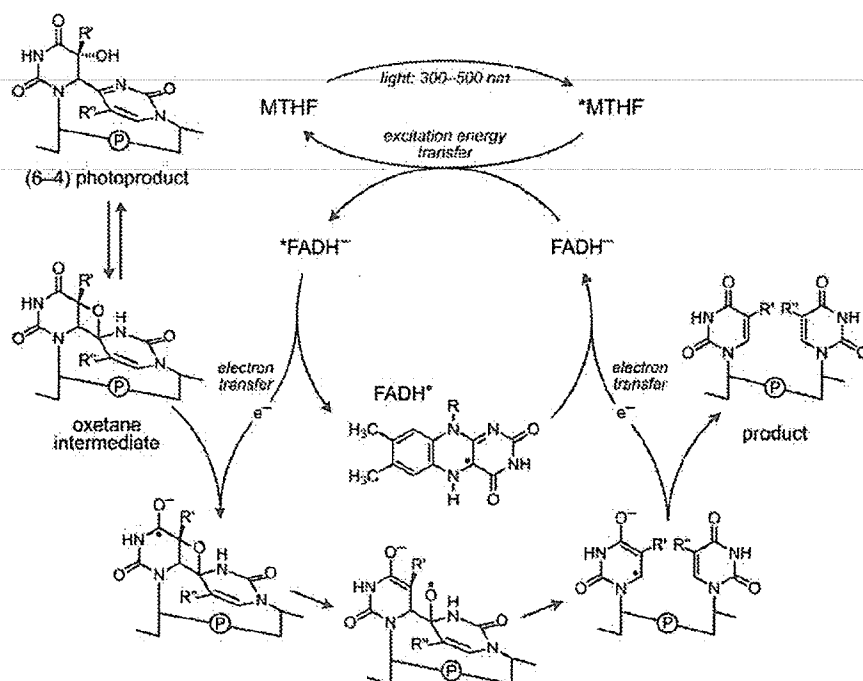


FIGURE 1. The proposed light-driven reaction mechanism for the repair of (6-4) photoproducts in DNA by (6-4) photolyase. *R* denotes the ribityl side chain of the FAD cofactor. *R'* and *R''* are either CH₃ in thymine or H in uracil. MTHF is the light-harvesting chromophore 5,10-methenyltetrahydrofolylpolyglutamate.

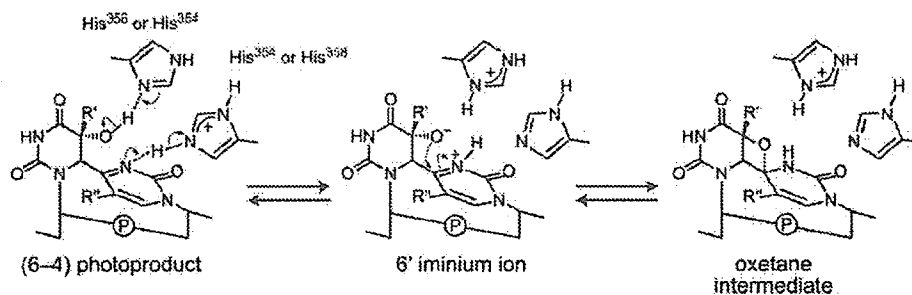


FIGURE 2. The proposed mechanism for oxetane intermediate formation in *X. laevis* (6-4) photolyase. *R'* and *R''* are either CH₃ in thymine or H in uracil.

CPD photolyase and (6-4) photolyase (17–20). In this so-called photoactivation (also called flavin-cofactor photoreduction), photolyases undergo reversible electron transfer reactions via amino acid residues to stepwise reduce their flavin cofactors to FADH[•] (for recent reviews see Refs 5 and 21). With regard to its electronic state (22), the stable neutral radical form of the flavin (FADH[•]) is the electronic state involved in both cofactor photoactivation and the catalytic repair of (6-4) photoproducts. Therefore, the characterization of FADH[•] leads to a better understanding of the individual steps of enzymatic DNA repair and furthermore is of considerable interest for comparative analyses of other flavoenzymes (23, 24) with reactive flavin radical intermediates.

Hyperexpression strains of *Escherichia coli* can generate large amounts of recombinant bacterial CPD photolyase in a catalytically inactive form characterized by intense absorption in the spectral range of 400–650 nm. This blue species contains a flavin radical that has been characterized in detail by EPR (25, 26). In contrast, recombinant *X. laevis* (6-4) photolyase expressed in *E. coli* is characterized by intense light absorption

in the range of 400–500 nm. The yellow species contains the flavin chromophore in its fully oxidized redox form (FAD^{ox}) (19).

In this study, the stable blue radical form (FADH[•]) of the flavin cofactor of (6-4) photolyase was generated by photoreduction of purified recombinant enzyme in the presence of an exogenously added electron donor, followed by aerial oxidation. This radical was examined by continuous-wave EPR spectroscopy and pulsed Davies-type electron nuclear double resonance (ENDOR). The hyperfine interactions arising from protons attached to the isoalloxazine moiety of the FAD cofactor were exploited to probe the immediate environment of the flavin, in particular hydrogen bonding and the micropolarity. The main focus of this study is to obtain information about the protonation states of His³⁵⁴ and His³⁵⁸, which are essential for DNA repair by (6-4) photolyase (16). This information is crucial for a thorough understanding of the light-independent catalytic steps preceding blue light-initiated enzymatic DNA repair, and the specific structural traits that distinguish (6-4) photolyase from the related CPD photolyase.

EXPERIMENTAL PROCEDURES

Protein Preparation—*X. laevis* wild-type and mutant (6-4) photolyases were overproduced in *E. coli*, purified as described previously (10, 19), and stored in liquid nitrogen. The concentration of the enzyme was determined on the basis of the oxidized FAD cofactor's absorbance at 450 nm ($\epsilon_{450} = 1.12 \times 10^4 \text{ M}^{-1} \text{ cm}^{-1}$) (10). For the present experiments, typically 0.5 mM (6-4) photolyase in a buffer containing 0.1 M NaCl, 0.05 M Tris-HCl (pH 6 to 9.5) and 30% (v/v) glycerol was used. The redox state of the flavin cofactor was monitored by recording the ground state optical absorption spectrum from 300 to 800 nm using a Shimadzu UV-1601PC spectrophotometer.

Preparation of a Stable Flavine Radical—Recombinantly produced oxidized (6-4) photolyase samples were supplemented with 10 mM EDTA, illuminated at 4 °C for 1 min with blue light (Halolux 30HL, Streppel, Wermelskirchen-Tente, Germany) selected with a 420–470-nm band filter (Schott, Mainz), and then incubated for about 20 min at 4 °C with air to reoxidize the light-generated dihydroflavin form of the flavin cofactor. The concentration of the resultant blue flavin radical (FADH[•]) was estimated based on its absorbance at 580 nm ($\epsilon_{580} = 0.48 \times 10^4 \text{ M}^{-1} \text{ cm}^{-1}$) (27).

ENDOR on (6-4) Photolyase

Buffer Exchange—Samples were transferred into the desired buffer (usually 0.1 M NaCl, 0.05 M Tris·HCl, or 0.05 M HEPES (pH 6–9.5) in 50% (v/v) glycerol) by dilution and ultrafiltration through Amicon C30 microconcentrators at 4 °C. Experiments in D₂O were carried out at pH 8.0 (uncorrected glass electrode reading) by performing a gel filtration chromatography step (HiPrep Desalting, GE Healthcare) at 4 °C.

EPR Sample Preparation—The enzyme preparations were transferred into EPR quartz tubes (3 mm inner diameter) under an argon inert-gas atmosphere in the dark. The enzyme was frozen rapidly with liquid nitrogen and stored therein. No changes in the signal line shape and intensity have been observed over a period of several months.

EPR/ENDOR Instrumentation—Continuous-wave X-band (microwave frequency, 9.67 GHz/magnetic field, ≈0.345 T) EPR spectra were obtained using a laboratory-built spectrometer described previously (25). X-band pulsed ENDOR spectra were recorded using a commercial pulse EPR spectrometer Bruker E580 (Bruker BioSpin GmbH, Rheinstetten, Germany) in conjunction with a dielectric-ring ENDOR resonator Bruker ER 4118X-MD5-EN. For Davies-type ENDOR (28), a microwave pulse sequence π - t - $\pi/2$ - τ - π using 64- and 128-ns $\pi/2$ - and π -pulses, respectively, and a radio frequency pulse of a 10- μ s duration starting 1 μ s after the first microwave pulse was used. The separation times t and τ between the microwave pulses were set to 13 μ s and 500 ns, respectively. To avoid saturation effects because of long relaxation times, the entire pulse pattern was repeated with a frequency of only 200 Hz.

ENDOR Spectra Analysis—For doublet state radicals, two ENDOR lines were expected per group of magnetically equivalent nuclei according to the first-order resonance condition, $\nu_{\text{ENDOR}}^{\pm} = |\nu_n \pm (A/2)|$, where $\nu_n = g_n \beta_n B_0 / h$ is the Larmor precessional frequency of the nucleus at the respective magnetic field B_0 , and g_n and β_n are the nuclear g values and the Bohr magnetons, respectively. In the weak coupling case, $|A| < 2|\nu_n|$, the separation of the line pair is determined by the orientation-dependent hyperfine coupling constant, A , that quantifies the interaction of the nuclear magnetic moment with the electron magnetic moment.

The hyperfine couplings from so-called α -protons bonded directly to π -conjugated carbon (or nitrogen) atoms are typically anisotropic, and the interaction symmetry is rhombic, *i.e.* $A_x \neq A_y \neq A_z$, where x , y , and z are the principal axes of the hyperfine tensor. With respect to the C–H (or N–H) bond and the aromatic π -plane, x , y , and z are aligned along the C–H (or N–H) bond, in-plane perpendicular to the C–H (or N–H) bond and parallel to the plane normal, respectively. If one extracts the isotropic part $A_{\text{iso}} = (A_x + A_y + A_z)/3$ from the tensor, the traceless anisotropic hyperfine contributions remain $T_i = A_i - A_{\text{iso}}$, $i \in \{x, y, z\}$. These are largely determined by the electron-nuclear dipolar interaction. Following arguments outlined previously for the N⁵-H⁵ fragment in FADH[•] (26), short N–H bond lengths lead to a symmetric rhombic hyperfine tensor with $T_z \rightarrow 0$ and $T_x = -T_y$. When the N-to-H bond length is increased, *e.g.* as a result of hydrogen bonding of the flavin to the protein backbone, the hyperfine tensor is expected to become more axially symmetric with $T_x = T_y = T_{\perp}$, and $T_z = T_{\parallel} \rightarrow -2T_{\perp}$.

The isotropic hyperfine coupling of a β -proton is related to the spin density ρ_X^{π} of the neighboring carbon ($X = \text{C}$) or nitrogen ($X = \text{N}$) atom in the π -plane, and according to the McConnell relation (29–32), $A_{\text{iso}}(\text{H}^{\beta}) = \rho_X^{\pi}(B' + B''\cos^2\theta)$, depends on the spatial orientation of the side chain. From the two empirical constants, B' and B'' , B' is typically very small, *i.e.* $B' \approx 0$. θ is the dihedral angle between the plane normal of the π -system and the projected C ^{β} H ^{β} bond. The hyperfine anisotropy of β -protons is typically small and approaches axial symmetry: $T_x \approx T_y = T_{\perp}$, $T_z = T_{\parallel}$.

Spectral Simulations—For ENDOR spectral simulations, the signal amplitudes were normalized to the integral of the signal arising from the hyperfine coupling of H⁶ in FADH[•]. This proton is nonexchangeable, and hence, the intensity of its ENDOR signal is expected to remain constant throughout different buffer conditions. Furthermore, H⁶ is more than 1 nm distant from the proposed substrate-binding pocket. Hence, changes of the protonation states of the histidines close to the substrate-binding site are not expected to alter the intensity or shape of the H⁶ ENDOR signal pair. To precisely extract the principal values of the hyperfine couplings of the H^{8 α} and H¹⁷ probes from the ENDOR data, spectral simulations were performed using the EPR spectral simulation software EasySpin (33) in conjunction with the MATLAB routine lsqcurvefit (The MathWorks, Natick, MA). This program calculates ENDOR powder spectra arising from two hyperfine tensors and fits their principal values to achieve the best possible agreement with the experimental data.

RESULTS

UV-visible Spectroscopic Analyses of the Flavin Cofactor Redox State—FAD cofactors often show characteristic optical absorption properties in all three biologically relevant redox states as follows: fully reduced (FADH[•] or FADH₂), semiquinone radical (FAD[•] or FADH[•]), and fully oxidized (FAD^{ox}). The (6-4) photolyase enzyme from *X. laevis* is isolated in a yellow form characteristic of a flavoprotein with a fully oxidized FAD^{ox}. The protein has absorption maxima at 448 and 366 nm that represent the S₀ → S₁ and S₀ → S₂ transitions of its flavin cofactor, respectively (Fig. 3). Well resolved vibration side bands at 425 and 475 nm and 356 and 372 nm, respectively, are indicative of tight and well defined noncovalent binding of the chromophore to the highly ordered protein structure. After illumination with blue light (420 < λ < 470 nm) in the presence of EDTA as an exogenous electron donor, the formation of the fully (two-electron) reduced FADH[•] form of the flavin chromophore is observed (see Fig. 3). A flavin radical, which exhibits absorption maxima at 590 and 635 nm, is subsequently generated by exposure of the enzyme to molecular oxygen. Residual absorbance at around 450 nm is because of flavin molecules that remained in the fully oxidized redox state because of incomplete flavin photoreduction. Under an inert gas atmosphere, the radical is stable on a time scale of hours, whereas back-reaction to the fully oxidized redox state occurs within minutes upon exposure of the enzyme to oxygen at room temperature (data not shown). The similarity of the optical absorption spectrum of the radical form of (6-4) photolyase to that obtained from the radical form of CPD photolyase (34) allows

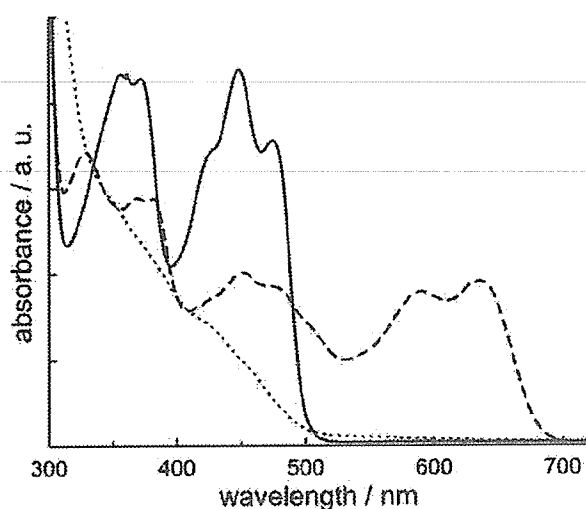


FIGURE 3. Optical absorption spectra of the (6-4) photolyase from *X. laevis* after enzyme isolation and purification before illumination (solid line), after photoreduction with EDTA (dotted line), and following subsequent exposure of the enzyme to oxygen (dashed line). Spectra were recorded at 298 K. a.u. indicates absorbance units.

us to conclude that in (6-4) photolyase the flavin radical is also present in the H^5 -protonated neutral form, $FADH^{\cdot}$. Typical for neutral flavin radicals are the absorption bands at 635 nm, which are assigned the $D_0 \rightarrow D_1$ transition, and the weak shoulder at around 510 nm that arises from the $D_0 \rightarrow D_2$ transition (35). A closer examination of the absorption spectrum of (6-4) photolyase reveals significant red shifts of 10, 10, and 13 nm for the red-most absorption bands at 590 and 635 nm relative to those of *E. coli*, yeast, and *Thermus thermophilus* CPD photolyase, respectively (34, 36, 37). Such bathochromic shifts in chromophores are normally caused by more extended delocalization of the π -electron system of aromatic molecules thus implying that $FADH^{\cdot}$ of (6-4) photolyase has altered electronic and hence redox properties as compared with the CPD photolyases, which could be important for its function.

Characterization of the Flavin Radical State by EPR Spectroscopy—To obtain a more detailed characterization of the electronic structure of the flavin radical in *X. laevis* (6-4) photolyase, EPR experiments were performed with a sample that was frozen in liquid nitrogen after generation of the flavin radical. The continuous-wave detected X-band EPR signal (see Fig. 4) reveals a radical signature centered at $g = 2.0034 \pm 0.0005$. The experimentally observed peak-to-peak line width of (2.00 ± 0.01) mT is typical of a neutral flavin radical, $FADH^{\cdot}$. The overall line width and the line shape of the signal are attributed to the mostly unresolved contributions of hyperfine couplings of the unpaired electron spin with 1H and ^{14}N nuclei of the isoalloxazine moiety of $FADH^{\cdot}$ as well as of the protein environment. Upon buffer deuteration, the exchangeable protons at N^5 and N^3 are replaced with deuterons. This results in a significant reduction of the inhomogeneous line width, which is clearly visible in Fig. 4.

Characterization of the Flavin Radical State by ENDOR Spectroscopy—We have performed ENDOR experiments to further characterize the electronic structure of the $FADH^{\cdot}$ cofactor in (6-4) photolyase. In Fig. 5, the X-band pulsed ENDOR spectrum of the $FADH^{\cdot}$ radical cofactor in protiated

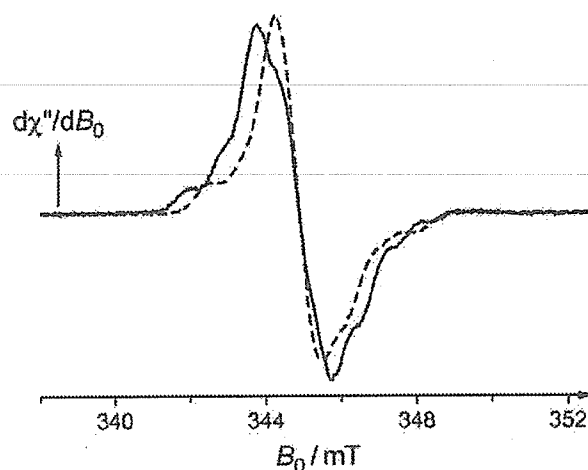


FIGURE 4. X-band (9.6703 GHz) frozen solution, continuous-wave-detected EPR spectrum of the FAD cofactor of *X. laevis* (6-4) photolyase in protiated (solid line) and deuterated (dashed line) buffer. The spectra were recorded at 80 K with a microwave power of 8 microwatts and a magnetic field modulation amplitude of 0.1 mT (modulation frequency, 100 kHz).

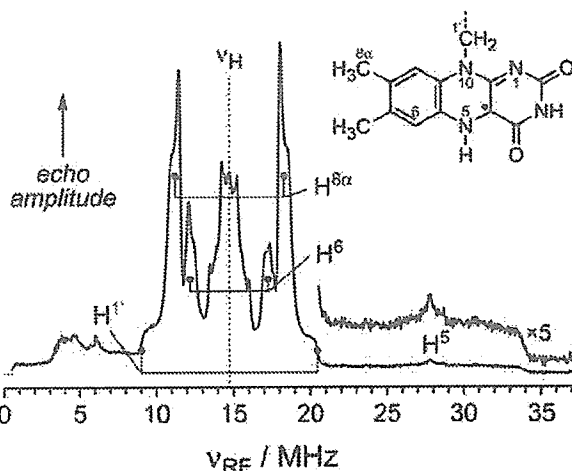


FIGURE 5. X-band frozen solution, proton-pulsed (Davies) ENDOR spectrum of the flavin cofactor of *X. laevis* (6-4) photolyase in protiated buffer recorded at the center magnetic field position (346.43 mT, 9.7138 GHz) in the EPR signal (see Fig. 4).

buffer is shown. The spectrum was recorded at a magnetic field value corresponding to the center magnetic field position of the X-band continuous-wave EPR signal shown in Fig. 4. In brief, ENDOR signals in five spectral regions between 1 and 37 MHz can be identified. Nearly all signals in this range are symmetrically distributed in pairs around the free proton Larmor frequency, $\nu_H = 14.75$ MHz. Hence, most proton hyperfine couplings are detected in the weak-coupling limit.

(i) The central so-called matrix-ENDOR signal extends from about 13.2 to 16.2 MHz and includes hyperfine couplings from protons whose nuclear spins are only weakly interacting with the unpaired electron spin, which is delocalized over the aromatic π -plane of the $FADH^{\cdot}$ isoalloxazine moiety. Small hyperfine couplings originate from protons in the protein backbone within the cofactor binding pocket, from protons of water molecules surrounding the flavin, and also from weakly coupled protons directly attached to the 7,8-dimethyl isoalloxazine ring, namely H^3 , $H^{7\alpha}$, and H^9 .

ENDOR on (6-4) Photolyase

(ii) Two prominent features are observed in the flanking 10.5–12- and 17.5–19-MHz radio frequency ranges. The tensorial line shapes are of almost axial symmetry and arise from the hyperfine couplings of the β -protons of the methyl group attached to C⁸. Typically, methyl groups rotate about their C–C bond at elevated temperatures. Hence, if this rotation is fast on the ENDOR time scale, one common hyperfine tensor for all three protons of the methyl group is observed. Signals of the H^{8 α} hyperfine tensor are in general easily detected in proton-ENDOR spectroscopy on flavins (25, 38–41) and are considered to be sensitive probes of the electron spin density on the outer xylene ring of the flavin isoalloxazine moiety (see also below). Furthermore, theory shows that the size of this coupling responds sensitively to polarity changes of the protein surroundings (42).

(iii) Flanking the H^{8 α} signals at around 9–10.5 and 19–20.5 MHz are found the transitions of one of the two β -protons, H^{1'}, attached to C^{1'} in the ribityl side chain of the isoalloxazine ring. In flavins, an analysis of this hyperfine coupling together with the one from the weaker-coupled second β -proton at C^{1'} yields information on the geometry of the ribityl chain attached to N¹⁰ as has been shown for the case of *E. coli* CPD photolyase (25).

(iv) Signals arising from the hyperfine coupling of the H⁶ proton are found at around 12 and 17.5 MHz. These show a small hyperfine anisotropy, in line with recent quantum-chemical calculations (22, 43).

(v) The broad feature extending from 21 to 34 MHz in the pulsed ENDOR spectrum is typically not observed in continuous-wave ENDOR experiments (25, 26). Its counterpart spanning the corresponding low radio frequency range is not resolved because of the overlap with ENDOR signals of the nitrogen nuclei. The broad 21–34-MHz pulsed ENDOR signal disappears when the enzyme is transferred from protiated into deuterated buffer (data not shown) (26). The symmetry of the underlying hyperfine coupling is clearly rhombic, *i.e.* $A_x \neq A_y \neq A_z$. As inferred from EPR spectroscopy and quantum-chemical calculations (22), this hyperfine coupling in the pulsed ENDOR spectrum is assigned to the proton bound to N⁵ (44). Its contribution to the overall spectrum is easily discriminated from that of other protons in the isoalloxazine moiety because of the exchangeability of H⁵ with a deuterium upon buffer deuteration. The only other exchangeable proton in the isoalloxazine moiety of flavins is that at N³. Its hyperfine coupling, however, is considerably smaller than that of H⁵, as has been shown by previous ENDOR experiments and quantum-chemical calculations (22). The amplitude and the anisotropy of the H⁵ hyperfine coupling has been shown recently to yield information on the strength of hydrogen bonding at H⁵ of the flavin to the protein backbone (26). The A_z and A_y components of this coupling are easily extracted from the peak position of the proton-ENDOR signal and the outer inflection point of the tensor pattern, respectively. The value of the A_x component has been obtained from deuterium ENDOR (44).

In Table 1, the proton hyperfine couplings from *X. laevis* (6-4) photolyase that have been obtained from pulsed ENDOR spectroscopy are summarized and compared with the proton hyperfine couplings of *E. coli* CPD photolyase.

TABLE 1

Proton hyperfine coupling constants of the FADH⁺ cofactors in *X. laevis* (6-4) photolyase and *E. coli* CPD photolyase obtained from pulsed ENDOR spectroscopy and pulsed and continuous-wave ENDOR spectroscopy, respectively

All values are given in MHz. Experimental errors are ± 0.1 MHz. The signs of hyperfine couplings have not been determined experimentally but were taken from theoretical considerations (22). The principal axes (x , y , and z) of the H⁵ hyperfine tensor are oriented as described in the text (26).

Atom		<i>X. laevis</i> (6-4) photolyase	<i>E. coli</i> CPD photolyase
H ⁵	A ^x	(–)13.7 ^a	(–)8.5 ^b
	A ^y	(–)38.4	(–)37.0 ^b
	A ^z	(–)26.1	(–)24.9 ^b
H ⁶	A _{iso}	(–)26.1	(–)23.5 ^b
	A ₁	(–)4.24	
	A ₂	(–)5.42	
H ^{8α}	A _{iso}	(–)4.65	–4.86 ^c
	A ₁	(+)6.50	(+)6.97 ^c
	A ₂	(+)8.13	(+)8.52 ^c
H ^{1'}	A _{iso}	(+)7.04	(+)7.49 ^c
	A ₁	(+)7.15	(+)7.9 ^c
	A ₂	(+)7.93	(+)7.9 ^c
	A ₃	(+)11.46	(+)11.3 ^c
	A _{iso}	(+)8.85	(+)9.0 ^c

^aData were scaled from deuterium ENDOR (44).

^bData were from Ref. 26.

^cData were from Ref. 25.

The pH Dependence of the H^{8 α} Hyperfine Coupling—Two histidines, His³⁵⁴ and His³⁵⁸, in *X. laevis* (6-4) photolyase that are unique to (6-4) photolyases (and consequently are not found in CPD photolyases) are critical for DNA repair activity. These histidines were proposed to play a pivotal role in the formation of the oxetane intermediate from the (6-4) photoproduct (Fig. 2), a step that is believed to occur prior to light-induced reductive cleavage (16). A theoretical structure model of (6-4) photolyase, which was built based on the crystallographic structure of *E. coli* CPD photolyase (45), suggests that these histidines are located close to (~ 0.4 nm) the 8 α -methyl group of the isoalloxazine moiety. Furthermore, if these histidines indeed play a functional role, then one would expect that changing the pH might readily cause a change of their protonation state. To test this model, we have recorded pulsed ENDOR spectra for the wild-type enzyme over the pH range between 6 and 9.5.

In Fig. 6, a series of difference ENDOR spectra for the wild-type protein as a function of pH are depicted. In the spectral region where the H^{8 α} protons show resonances, significant spectral shifts and intensity changes are observed. Other differences are mostly restricted to the matrix-ENDOR, region but they are very small. Notably, the signals of the other protons such as H⁶ or H⁵ remain virtually unchanged. Hence, in the following Figs. 7 and 8, we only show the high frequency parts of the ENDOR spectra in the 17.8–21.2-MHz range. These spectra were normalized with respect to the ENDOR signal of H⁶. It is immediately apparent that the intensity of the H^{8 α} ENDOR signal changes significantly as a function of pH (see Fig. 7, panel A). Similar experiments carried out with HEPES-buffered protein in order to exclude potential buffer-dependent artifacts (46) yielded virtually identical results.

For data analysis, it has to be taken into account that the signal of H^{8 α} overlaps with the one arising from H^{1'}. We have therefore simulated the data from Fig. 7, panel A, using a least squares fitting program that calculates ENDOR spectra arising from these two nonequivalent protons with anisotropic hyperfine tensors. In the simulations, the hyperfine principal values

of both tensors were then adjusted such that the best possible agreement with the experimental data was obtained. As an illustration, the experimental and simulated ENDOR spectra of the wild-type enzyme recorded at pH 8 are shown in Fig. 7, *panel B*. In general, the agreement between experiment and simulation is excellent. Thus precise principal values for the two hyperfine tensors of $H^{8\alpha}$ and $H^{1'}$ could be obtained (see Table 2). Both the principal values of the $H^{8\alpha}$ hyperfine coupling tensor and the overall signal intensity (the integral over the entire tensorial pattern; see Fig. 7, *panel C*) are affected by changes of the pH. This is not unexpected because it is well documented that changes in the micropolarity or the pH of the surroundings of a paramagnetic molecule may alter both the hyperfine couplings and the relaxation behavior of the nuclei (47–50). Furthermore, changes in pH often cause small but distinct geometrical reorientations of protein side chains. These structural changes may influence the free rotation of methyl groups. When the motion is fast on the time scale of the

observer, the hyperfine couplings of the three protons coalesce and average to give a single purely axial hyperfine coupling tensor. When the motion slows, the averaging is incomplete, thus rendering the tensor slightly rhombic.

Two mutant proteins, H354A and H358A, were also examined by pulsed ENDOR spectroscopy at two extreme pH values, pH 6 and 9.5, to identify the origin of the pH dependence of the principal values of the $H^{8\alpha}$ hyperfine tensor. Both mutant enzymes are inactive in photorepair (16), but the photoreduction reaction is still possible. In Fig. 8, the pulsed ENDOR spectra and the spectral simulations for the mutant proteins are shown and compared with the data from the wild type. A comparison of the wild type and the mutants at different pH conditions reveals characteristic differences both in the hyperfine principal values and the signal intensities.

For the wild-type enzyme, the ENDOR signal arising from the $H^{8\alpha}$ hyperfine coupling has axial symmetry, i.e. $A_1(H^{8\alpha}) = A_2(H^{8\alpha}) \equiv A_{\perp}(H^{8\alpha})$ and $A_3(H^{8\alpha}) \equiv A_{\parallel}(H^{8\alpha})$ (see Table 2) as is expected for a rapid (on the ENDOR time scale) methyl group rotation about the $C^{\beta}-C^{8\alpha}$ bond in FADH $^{\cdot}$. The $H^{1'}$ hyperfine coupling tensor on the other hand is slightly rhombic, $A_1(H^{1'}) \neq A_2(H^{1'}) \neq A_3(H^{1'})$ as is predicted from quantum-chemical calculations (22). Within experimental error, the principal values of the hyperfine tensors of $H^{8\alpha}$ and $H^{1'}$ remain constant from pH 9.5 to pH 6. In contrast, the signal intensity of $H^{8\alpha}$ is pH-dependent with an observed maximum at pH 7.

The overall shapes of the ENDOR spectra of the H358A mutant protein largely resemble those of the wild type at the respective pH conditions. The slight rhombicity of the $H^{8\alpha}$ hyperfine splitting measured at pH 9.5 reveals a perturbation of the flavin-binding site at this position induced by the replacement of His 358 by alanine. Furthermore, the isotropic hyperfine coupling of $H^{8\alpha}$ at pH 9.5 (Table 2) increases from 7.05 MHz (wild type) to 7.16 MHz (H358A) indicating that the modification of the environment renders the surroundings of $H^{8\alpha}$ slightly more polar. The small shift observed in the hyperfine coupling of $H^{1'}$ likely reflects a small reorientation of the ribityl side chain, although no appreciable changes in the principal values of the hyperfine tensor are observed upon reduction of the buffer pH.

The H354A protein, in contrast to the wild type or the H358A mutant, exhibits significant pH-dependent changes in its ENDOR spectra (Fig. 8). At pH 9.5, a substantial reduction of the $H^{1'}$ hyperfine coupling is observed accompanied by a clear symmetry change of the $H^{8\alpha}$ signal. Furthermore, the principal hyperfine values of both protons change significantly upon altering the pH. Thus replacement of His 354 with alanine leads to significant modifications of the cofactor-binding site at the 8α -methyl group and at the linkage of the ribityl side chain. These modifications render the principal components of

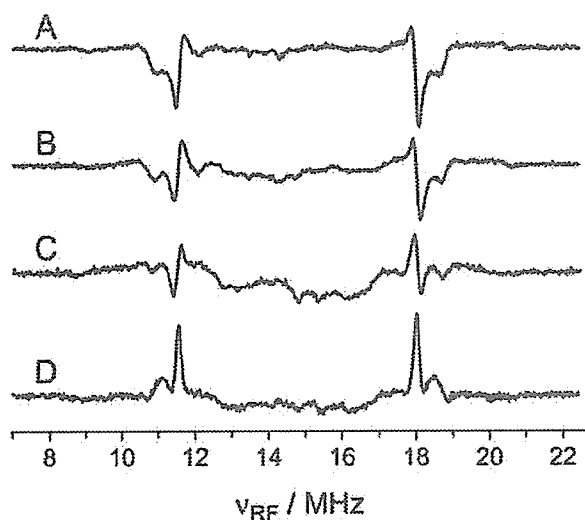


FIGURE 6. Difference X-band frozen solution, proton-pulsed (Davies) ENDOR spectra of the flavin cofactor of *X. laevis* (6-4) photolyase in protonated buffer. Panel A, pH 6–pH 7; panel B, pH 6–pH 8; panel C, pH 6–pH 9; panel D, pH 6–pH 9.5.

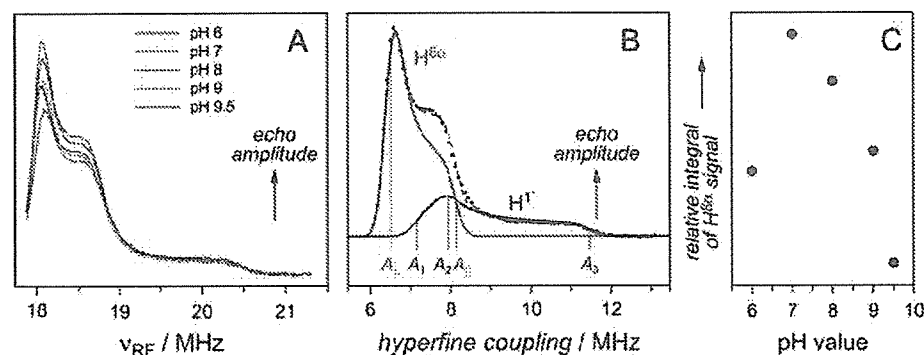


FIGURE 7. X-band (9.7318 GHz) frozen solution (80 K), pulsed ENDOR spectra of FADH $^{\cdot}$ bound to wild-type *X. laevis* (6-4) photolyase. All experimental spectra were recorded at a magnetic field of 347.07 mT. Panel A, pulsed ENDOR spectra recorded at different pH values as follows: pH 6 (blue curve), pH 7 (green curve), pH 8 (red curve), pH 9 (turquoise curve), and pH 9.5 (magenta curve). Panel B, experimental (dots) and simulated (dashed line) pulsed ENDOR spectra of wild-type *X. laevis* (6-4) photolyase (pH 8.0). The red and the blue curves show the contributions of the $H^{8\alpha}$ and the $H^{1'}$ hyperfine couplings to the calculated ENDOR spectrum, respectively. Panel C, the integral over the $H^{8\alpha}$ hyperfine contribution as a function of the pH value.

ENDOR on (6-4) Photolyase

the $H^{8\alpha}$ hyperfine tensor more sensitive to pH changes as compared with the wild-type enzyme and the H358A mutant. Virtually identical results were obtained from samples where the pH has been adjusted by HEPES instead of Tris buffer.

DISCUSSION

Comparison of the Electronic Structure of the Neutral Flavin Radicals in (6-4) Photolyase and CPD Photolyase—Differences in the proton hyperfine couplings of $FADH^{\cdot}$ bound to (6-4) photolyase versus CPD photolyase (Table 1) can be interpreted in light of sequence and proposed structural differences in the flavin-binding sites of these DNA repair enzymes. Isotropic hyperfine couplings of α - and β -protons of aromatic radicals, such as $FADH^{\cdot}$, reflect the unpaired electron spin density on the carbons and nitrogens to which they are bonded. This electron spin density distribution in turn reflects the protein environment. In Fig. 9, the amino acid alignment of the C-terminal parts of *E. coli* CPD photolyase and *X. laevis* (6-4) photolyase highlights the 14 amino acids within 0.5 nm of the isoalloxazine moiety of $FADH^{\cdot}$ in *E. coli* CPD photolyase (45). Nine of these

14 are conserved in *X. laevis* (6-4) photolyase; two have similar electronic properties, and three are dissimilar. Among the (6-4) photolyases, two of these are highly conserved histidines (His³⁵⁴ and His³⁵⁸ in *X. laevis*), and the third is the polar Asn³⁹⁴ (*X. laevis*) replacing of Gly³⁸¹ in CPD photolyase (*E. coli*).

$H^{8\alpha}$ -proton hyperfine coupling is known to be an excellent probe for sensing subtle differences in the surroundings of the xylene region of the isoalloxazine up to distances of about 0.6 nm (39, 42). The size of the $H^{8\alpha}$ coupling depends on the micropolarity as well as on the aromaticity of the amino acids binding the flavin. Although the $H^{8\alpha}$ -proton hyperfine coupling of $FADH^{\cdot}$ in *E. coli* CPD photolyase is one of the smallest reported for an enzyme with a neutral flavin radical (25, 40), that of $FADH^{\cdot}$ in (6-4) photolyase is even smaller (see Table 1). This decrease in $H^{8\alpha}$ -proton hyperfine coupling implies a less polar and/or more aromatic environment for $FADH^{\cdot}$ in (6-4) photolyase, due to one or both of the following changes: (i) a smaller substrate-binding pocket for (6-4) photolyase that would limit the number of water molecules that could approach the redox-active flavin cofactor in the absence of a DNA lesion; and (ii) the two aromatic histidine residues, His³⁵⁴ and His³⁵⁸, predicted to replace nonaromatic Asn and Met in the *E. coli* CPD photolyase active site (16).

Analysis of the crystal structure of a CPD photolyase bound to a repaired CPD-damaged DNA double strand showed that the 8 α -methyl group of FAD is oriented toward the substrate binding cavity (51). The structure of (6-4) photolyase is predicted to be largely similar (16); however, because of the different geometry of the (6-4) photoproduct (52, 53), one would expect a smaller substrate cavity as compared with the CPD photolyase. We have previously shown that the displacement of water molecules upon substrate binding to *E. coli* CPD photolyase alters the polarity of the flavin cofactor surroundings (42). In these experiments, however, the proton hyperfine shifts detected upon binding of a DNA substrate were minute; the isotropic hyperfine coupling of $H^{8\alpha}$ in substrate-bound photolyase was only about 1% smaller than that of the free enzyme. Thus, it is very likely that the small $H^{8\alpha}$ hyperfine coupling in (6-4) photolyase is predominantly because of differences in the immediate environment of $H^{8\alpha}$ introduced by His³⁵⁴ and His³⁵⁸, rather than to the smaller substrate cavity.

Hydrogen Bonding of the Flavin Chromophore to the Protein Environment—By further inspection of the hyperfine couplings of $FADH^{\cdot}$ listed in Table 1, and by comparison of these values

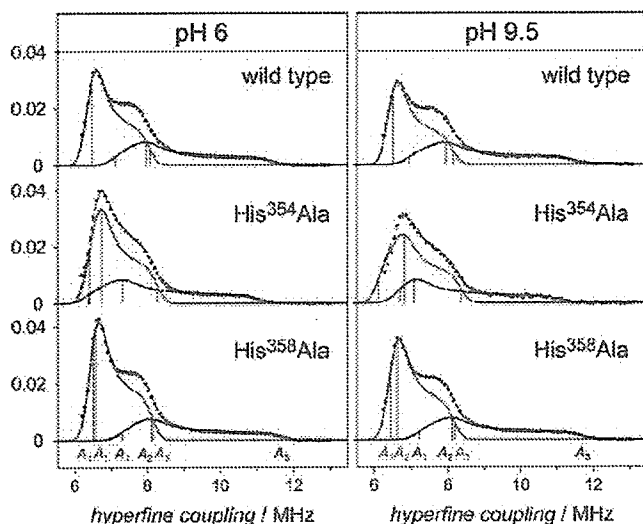


FIGURE 8. X-band (9.7318 GHz) frozen solution (80 K), pulsed ENDOR spectra of $FADH^{\cdot}$ bound to wild-type and mutant *X. laevis* (6-4) photolyases at different pH values. All experimental spectra (dots) were recorded at a magnetic field of 347.07 mT. The simulations have been performed using the parameters given in Table 2. The red and the blue curves show the contributions of the $H^{8\alpha}$ and the H^1 hyperfine couplings to the overall calculated ENDOR (dashed black curves) spectra, respectively. The vertical lines show the positions of the principal hyperfine components of the hyperfine tensors.

TABLE 2

$H^{8\alpha}$ and H^1 proton hyperfine couplings of the $FADH^{\cdot}$ cofactors obtained from simulations of the pulsed ENDOR spectra of wild-type and mutant *X. laevis* (6-4) photolyase at different pH values

All values are in MHz; signs of hyperfine couplings have not been determined experimentally but were taken from theoretical calculations. The experimental errors are ± 0.02 MHz for the A_3 components, and ± 0.04 MHz for the A_1 and A_2 components.

Protein	$H^{8\alpha}$						H^1					
	pH 6			pH 9.5			pH 6			pH 9.5		
Wild type	A_1	6.46	A_{iso} 7.00	A_1	6.50	A_{iso} 7.05	A_1	7.10	A_{iso} 8.82	A_1	6.95	A_{iso} 8.80
	A_2	6.46		A_2	6.50		A_2	7.96		A_2	7.94	
	A_3	8.07		A_3	8.14		A_3	11.39		A_3	11.51	
H354A	A_1	6.43	A_{iso} 7.17	A_1	6.14	A_{iso} 7.11	A_1	6.40	A_{iso} 8.28	A_1	6.72	A_{iso} 8.31
	A_2	6.76		A_2	6.83		A_2	7.35		A_2	7.11	
	A_3	8.32		A_3	8.37		A_3	11.08		A_3	11.10	
H358A	A_1	6.58	A_{iso} 7.15	A_1	6.52	A_{iso} 7.16	A_1	7.38	A_{iso} 9.10	A_1	7.30	A_{iso} 9.09
	A_2	6.64		A_2	6.71		A_2	8.18		A_2	8.20	
	A_3	8.24		A_3	8.26		A_3	11.73		A_3	11.78	



FIGURE 9. Alignment of the amino acid sequences of *E. coli* CPD photolyase and *X. laevis* (6-4) photolyase. Residues within a distance of 0.5 nm from the isoalloxazine of the respective FAD cofactor in *E. coli* CPD photolyase (45) are marked with asterisks. Conserved amino acids are shaded in black; similar residues in terms of the electronic properties of their side chains are shaded in gray. Dissimilar amino acids in the FAD binding domains of both photolyases are marked with a #.

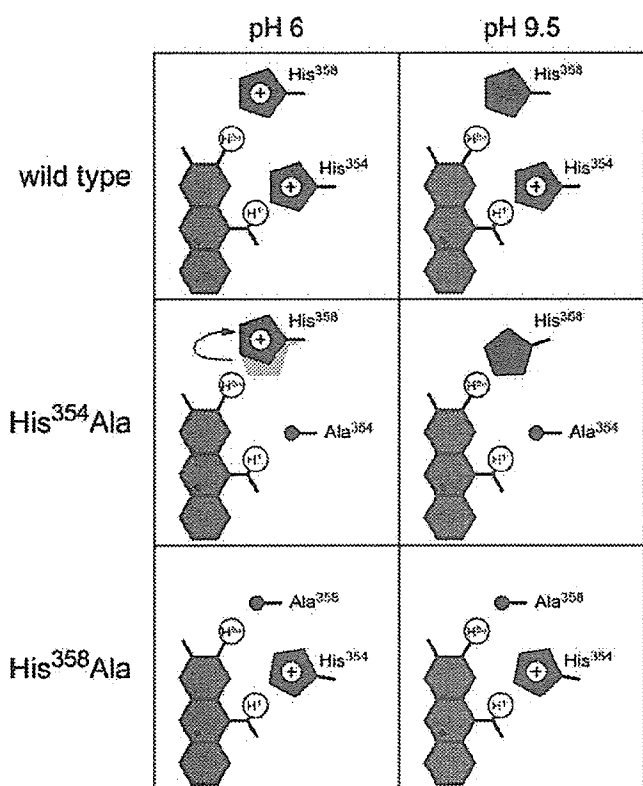


FIGURE 10. Proposed changes in the microenvironment of $H^{6\alpha}$ and $H^{1'}$ introduced by point mutations and pH changes. For details, see text.

with the corresponding couplings from *E. coli* CPD photolyase, more conclusions can be drawn. The respective values of the proton hyperfine couplings from H^6 and $H^{1'}$ are almost identical, implying that the unpaired electron spin density at C^6 and the geometry of the ribityl side-chain attachment are very similar in both enzymes. The isotropic hyperfine coupling of H^5 , however, is significantly larger in (6-4) photolyase (-26.1 MHz) than in its counterpart CPD photolyase (-23.5 MHz). Furthermore, the symmetry of the H^5 hyperfine tensor is different. An analysis of its anisotropy reveals the components $T_x = -T_y = 12.4$ MHz and $T_z = 0$ for (6-4) photolyase. Such values are indicative for a shortened N-H bond as compared with CPD photolyase, thus implying that the expected hydrogen bond of an amino acid to H^5 is weaker in *X. laevis* (6-4) photolyase

than in *E. coli* CPD photolyase ($T_x = 15.0$ MHz; $T_y = -13.5$ MHz; $T_z = -1.4$ MHz). Within 0.5 nm around H^5 , however, no changes in the amino acid alignment are observed (see Fig. 9). Therefore, this pronounced effect must be due to minor changes in the spatial arrangement of the hydrogen bond forming amino acid Asn³⁹² and H^5 . Interestingly, a weakened hydrogen bond $N^5-H^5 \cdots O(\text{Asn}^{392})$ in (6-4) photolyase, and hence a shorter N-H bond, also correlates with the observed red shifts (13 nm as compared with *E. coli* CPD photolyase) in the optical absorbance bands. Although on a smaller scale, this effect parallels the dramatic red shift of the longest wavelength optical absorptions observed when going from the N^5 -deprotonated anion radical, $FAD^{\cdot-}$, to the neutral radical, $FADH^{\cdot}$. Thus, in anionic flavin radicals, the electron in the singly occupied molecular orbital more confined to the outer xylene ring and hence the larger $H^{6\alpha}$ hyperfine couplings are typically observed. In neutral flavin radicals, on the other hand, the electron in the singly occupied molecular orbital is more shifted toward the central pyrazine ring thus leading to smaller $H^{6\alpha}$ hyperfine couplings. Similar conclusions have been recently drawn from results of a resonance Raman study of *Arabidopsis thaliana* (6-4) photolyase (54).

The Positions and Protonation States of the Functional Histidines His³⁵⁴ and His³⁵⁸—In 1994, Kim *et al.* (14) proposed that formation of a four-membered ring intermediate precedes thymine-dimer splitting in (6-4) photolyase. Later it was suggested that two highly conserved histidines His³⁵⁴ and His³⁵⁸ catalyze the formation of this oxetane intermediate (16). (6-4) photolyases, in contrast to CPD photolyases, exhibit a pronounced pH dependence for DNA repair. The repair activity is highest at around pH 9; the reaction rate decreases by nearly 50% at pH 7 (16). The interpretation of this phenomenon led to discussions about the protonation states of His³⁵⁴ and/or His³⁵⁸. Because the function of histidine is markedly influenced by its protonation state, it is likely that the histidines at the solvent-exposed active site cause the unusual pH dependence in the (6-4) photolyase repair activity *in vitro* (16). The protonation of a histidine alters its polarity, which may be indirectly probed by proton-ENDOR spectroscopy using $FADH^{\cdot}$ as an observer. The principal values of the hyperfine coupling tensors of $H^{1'}$ and $H^{6\alpha}$, the symmetry of their hyperfine interaction, and the relaxation behavior of the nuclear spins as reflected in the ENDOR signal intensities depend on structural modifications introduced by point mutations and on the pH. Hence, proton-ENDOR experiments performed on the wild-type enzyme and the two mutant proteins, in which the two histidines are separately replaced by alanine, allow a detailed picture of the microenvironment at the putative substrate-binding site to be painted (Fig. 10).

No three-dimensional structure of a (6-4) photolyase enzyme is available to date, but the strong shift of the isotropic hyperfine coupling of $H^{1'}$ in H354A, as compared with the wild type

ENDOR on (6-4) Photolyase

or the H358A protein, both at pH 9.5 and pH 6 (see Fig. 8), suggests that His³⁵⁴ is close to H^{1'} (see Fig. 10). The changes in $A_{\text{iso}}(\text{H}^{1'})$ may be rationalized in terms of a ribityl side-chain reorientation, which happens when His³⁵⁴ is replaced by the smaller alanine. This reorientation results in an altered direction of the C^{1'}-H^{1'} bond with respect to the π -plane of the isoalloxazine ring, thus changing the dihedral angle θ (see above) and hence the H^{1'} hyperfine coupling. Only small changes on the H^{1'} coupling are observed in the H358A mutant, which shows that His³⁵⁸ must be further removed from H^{1'}.

At pH 9.5 the shift of the isotropic hyperfine coupling of H^{8 α} , with respect to the wild type, is larger in the H358A mutant than in H354A, which shows that His³⁵⁸ is located close to H^{8 α} . The line shape of the H^{8 α} ENDOR signal in the H354A mutant is quite different from that of the other two proteins. In H354A, a more rhombic symmetry is observed: $A_1 \neq A_2 \neq A_3$, whereas in the others the hyperfine tensor is nearly axial symmetric, i.e. $A_1 \approx A_2 \neq A_3$. Furthermore, the H^{8 α} ENDOR signal in the H354A mutant is also strongly pH-dependent, an effect that must originate from a protonation change of His³⁵⁸ when going from pH 9.5 to 6. For steric reasons, it is likely that at pH 9.5, the (deprotonated) His³⁵⁸ residue turns toward the smaller Ala³⁵⁴. The axial symmetry of the hyperfine tensor, which is due to free methyl group rotation in the wild type, might be affected by this His³⁵⁸ reorientation such that the rotation about the C⁸-C^{8 α} bond is hindered and thus the rhombicity of the H^{8 α} hyperfine coupling is increased. At pH 6, the H^{8 α} hyperfine coupling remains slightly rhombic, although the anisotropy between A_1 and A_2 is significantly reduced presumably due to a further reorientation of His³⁵⁸, which is protonated at pH 6 (Fig. 10). In the wild type, these effects are not observed presumably because reorientation of the histidine residue is not possible because of mutual direct or indirect hydrogen bonding.

The pH changes are also reflected in the signal intensities of the H^{8 α} hyperfine coupling. The integrals of this signal at two different pH values, pH 9.5 and 6, for all three proteins are compared graphically in Fig. 11.

In the wild type and the mutants, the H^{8 α} ENDOR signal intensity generally increases when going from pH 9.5 to pH 6 (see Figs. 7 and 8). However, although the wild type and the H354A mutant protein exhibit virtually the same intensity changes as the proton concentration is raised, the H^{8 α} ENDOR signal of the H358A mutant shows a larger increase (Fig. 11, panel A). This is more clearly observed if one corrects the gradients of H354A and H358A for the wild-type effect (Fig. 11, panel B). The same quantitative changes in the relaxation behavior of the H354A mutant and the wild type imply that His³⁵⁸ undergoes the same change of protonation state in both the wild-type and H354A mutant proteins. In the H358A mutant, His³⁵⁴ could be protonated at pH 6 and deprotonated at pH 9.5, but the effect of a possible protonation change on the H^{8 α} ENDOR signal is expected to be small because His³⁵⁴ is closer to H^{1'}. However, the principal values of the H^{1'} and H^{8 α} hyperfine couplings in the H358A mutant show (within experimental error) virtually no pH dependence. This implies that His³⁵⁴ does not change its protonation state when going from pH 9.5 to 6. Hence, the protonated histidine that catalyzes oxet-

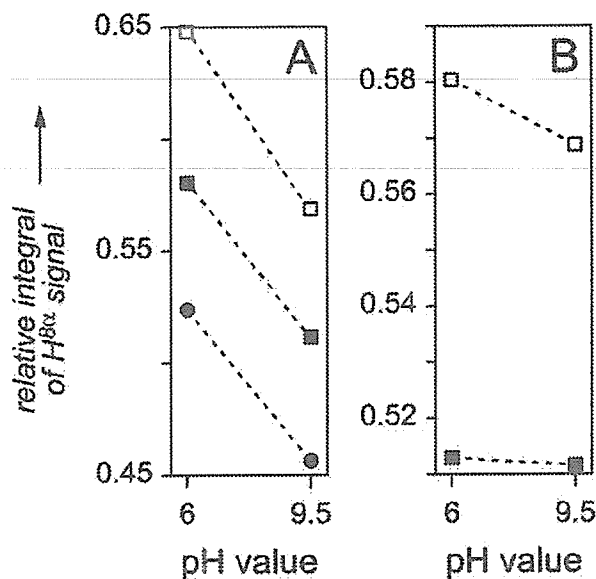


FIGURE 11. pH dependence of the H^{8 α} ENDOR signal intensities (see Fig. 9) of mutant and wild-type (6-4) photolyases. Panel A, relative signal intensities with respect to the normalized H⁶ ENDOR signal (in arbitrary units): wild-type (6-4) photolyase (circles); H354A (6-4) photolyase (filled squares); H358A (6-4) photolyase (open squares). Panel B, relative signal intensities corrected for the wild-type signal intensity changes: H354A (6-4) photolyase (filled squares); H358A (6-4) photolyase (open squares).

ane intermediate formation must be His³⁵⁴ because His³⁵⁸ is deprotonated at pH 9.5.

Conclusions—In the absence of an x-ray structure of (6-4) photolyase, an alignment of the amino acid sequences of *E. coli* CPD photolyase and *X. laevis* (6-4) photolyase has been used to suggest that the amino acids His³⁵⁸ and His³⁵⁴, which play a crucial role in DNA repair, are close to the flavin cofactor and replace Asn³⁴⁵ and Met³⁴¹ in *E. coli* CPD photolyase, for which the structure is known. Our spectroscopic data provide the first experimental evidence that this model is essentially correct; His³⁵⁴ is close to FAD H^{1'} and His³⁵⁸ is close to FAD H^{8 α} (Fig. 10). Furthermore, we showed that at pH 9, His³⁵⁸ is likely to be deprotonated, and His³⁵⁴ is protonated. Hence, His³⁵⁴ is proposed to be the protonated histidine that initiates formation of the oxetane intermediate from the (6-4) photoproduct (Fig. 2) in the enzymatic DNA repair reaction.

These conclusions are based on changes in the principal components and the intensities of selected hyperfine coupling tensors of the flavin radical caused by point mutations and pH. Simulation and deconvolution of pulsed ENDOR spectra have allowed complete tensorial patterns of H⁵, H⁶, H^{8 α} , and H^{1'} in a protein-bound neutral flavin radical to be resolved, showing that, in the present case, point mutations in the protein predominantly affect the hyperfine couplings of individual protons. Thus, pulsed-ENDOR examinations of flavoproteins provide far more information than is typically obtained by the continuous-wave ENDOR technique; the latter method is not well suited for the detection of broad lines arising from strong anisotropic proton hyperfine couplings such as those from H⁵ and H^{1'}. Thus, we expect that pulsed ENDOR will emerge as a potent tool to study the protonation states of amino acid residues located close to the cofactor in flavoproteins.

Acknowledgments—We thank Professor Robert Bittl (Freie Universität Berlin) for the use of the EPR instrumentation and critical reading of this manuscript. K. H. and E. D. G. thank Professors John A. Tainer (The Scripps Research Institute) and Shigenori Iwai (Osaka University) for generous encouragement.

REFERENCES

- Friedberg, E. C., Walker, G. C., and Siede, W. (1995) *DNA Repair and Mutagenesis*, American Society for Microbiology, Washington, D. C.
- Todo, T. (1999) *Mutat. Res.* **434**, 89–97
- Deisenhofer, J. (2000) *Mutat. Res.* **460**, 143–149
- Sancar, A. (2003) *Chem. Rev.* **103**, 2203–2237
- Weber, S. (2005) *Biochim. Biophys. Acta* **1707**, 1–23
- Essen, L.-O. (2006) *Curr. Opin. Struct. Biol.* **16**, 51–59
- Todo, T., Ryo, H., Yamamoto, K., Toh, H., Inui, T., Ayaki, H., Nomura, T., and Ikenaga, M. (1996) *Science* **272**, 109–112
- Nakajima, S., Sugiyama, M., Iwai, S., Hitomi, K., Otoshi, E., Kim, S.-T., Jiang, C.-Z., Todo, T., Britt, A. B., and Yamamoto, K. (1998) *Nucleic Acids Res.* **26**, 638–644
- Sancar, A., and Sancar, G. B. (1984) *J. Mol. Biol.* **172**, 223–227
- Todo, T., Kim, S.-T., Hitomi, K., Otoshi, E., Inui, T., Morioka, H., Kobayashi, I., Ohtsuka, E., Toh, H., and Ikenaga, M. (1997) *Nucleic Acids Res.* **25**, 764–768
- Jorns, M. S., Sancar, G. B., and Sancar, A. (1984) *Biochemistry* **23**, 2673–2679
- Eker, A. P. M., Kooiman, P., Hessels, J. K. C., and Yasui, A. (1990) *J. Biol. Chem.* **265**, 8009–8015
- Jordan, S. P., and Jorns, M. S. (1988) *Biochemistry* **27**, 8915–8923
- Kim, S.-T., Malhotra, K., Smith, C. A., Taylor, I.-S., and Sancar, A. (1994) *J. Biol. Chem.* **269**, 8535–8540
- Zhao, X., Liu, J., Hsu, D. S., Zhao, S., Taylor, J.-S., and Sancar, A. (1997) *J. Biol. Chem.* **272**, 32580–32590
- Hitomi, K., Nakamura, I. I., Kim, S.-T., Mizukoshi, T., Ishikawa, T., Iwai, S., and Todo, T. (2001) *J. Biol. Chem.* **276**, 10103–10109
- Heelis, P. F., Okamura, T., and Sancar, A. (1990) *Biochemistry* **29**, 5694–5698
- Li, Y. F., Heelis, P. F., and Sancar, A. (1991) *Biochemistry* **30**, 6322–6329
- Hitomi, K., Kim, S.-T., Iwai, S., Harima, N., Otoshi, E., Ikenaga, M., and Todo, T. (1997) *J. Biol. Chem.* **272**, 32591–32598
- Weber, S., Kay, C. W. M., Mögling, H., Möbius, K., Hitomi, K., and Todo, T. (2002) *Proc. Natl. Acad. Sci. U. S. A.* **99**, 1319–1322
- Byrdin, M., Sartor, V., Eker, A. P. M., Vos, M. H., Aubert, C., Brettel, K., and Mathis, P. (2004) *Biochim. Biophys. Acta* **1655**, 64–70
- Weber, S., Möbius, K., Richter, G., and Kay, C. W. M. (2001) *J. Am. Chem. Soc.* **123**, 3790–3798
- Kay, C. W. M., and Weber, S. (2002) in *Electron Paramagnetic Resonance* (Gilbert, B. C., Davies, M. J., and Murphy, D. M., eds) Vol. 18, pp. 222–253, Royal Society of Chemistry, Cambridge, UK
- Edmondson, D. E., and Tollin, G. (1983) *Top. Curr. Chem.* **108**, 109–138
- Kay, C. W. M., Feicht, R., Schulz, K., Sadewater, P., Sancar, A., Bacher, A., Möbius, K., Richter, G., and Weber, S. (1999) *Biochemistry* **38**, 16740–16748
- Weber, S., Kay, C. W. M., Bacher, A., Richter, G., and Bittl, R. (2005) *Chemphyschem.* **6**, 292–299
- Jorns, M. S., Wang, B., Jordan, S. P., and Chanderkar, L. P. (1990) *Biochemistry* **29**, 552–561
- Davies, E. R. (1974) *Phys. Lett. A* **47**, 1–2
- Carrington, A., and McLachlan, A. D. (1967) *Introduction to Magnetic Resonance*, pp. 83–85, Harper & Row, New York
- Heller, C., and McConnell, H. M. (1960) *J. Chem. Phys.* **32**, 1535–1539
- Stone, E. W., and Maki, A. H. (1962) *J. Chem. Phys.* **37**, 1326–1333
- Fasanella, E. L., and Gordy, W. (1969) *Proc. Natl. Acad. Sci. U. S. A.* **62**, 299–304
- Stoll, S., and Schweiger, A. (2006) *J. Magn. Reson.* **178**, 42–55
- Payne, G., Heelis, P. F., Rohrs, B. R., and Sancar, A. (1987) *Biochemistry* **26**, 7121–7127
- Schelvis, J. P. M., Ramsey, M., Sokolova, O., Tavares, C., Cecala, C., Connell, K., Wagner, S., and Gindt, Y. M. (2003) *J. Phys. Chem. B* **107**, 12352–12362
- Sancar, G. B., Smith, F. W., and Heelis, P. F. (1987) *J. Biol. Chem.* **262**, 15457–15465
- Kato, R., Hasegawa, K., Hidaka, Y., Kuramitsu, S., and Hoshino, T. (1997) *J. Bacteriol.* **179**, 6499–6503
- Kurreck, H., Bock, M., Bretz, N., Flisner, M., Kraus, H., Lubitz, W., Müller, F., Geissler, J., and Kroneck, P. M. H. (1984) *J. Am. Chem. Soc.* **106**, 737–746
- Medina, M., Lustao, A., Sancho, J., Gómez-Moreno, C., Cammack, R., Alonso, P. J., and Martínez, J. I. (1999) *Biophys. J.* **77**, 1712–1720
- Barquera, B., Morgan, J. E., Lukoyanov, D., Scholes, C. P., Gennis, R. B., and Nilges, M. J. (2003) *J. Am. Chem. Soc.* **125**, 265–275
- Kay, C. W. M., Schleicher, E., Kuppig, A., Hofner, H., Rüdiger, W., Schleicher, M., Fischer, M., Bacher, A., Weber, S., and Richter, G. (2003) *J. Biol. Chem.* **278**, 10973–10982
- Weber, S., Richter, G., Schleicher, E., Bacher, A., Möbius, K., and Kay, C. W. M. (2001) *Biophys. J.* **81**, 1195–1204
- García, J. I., Medina, M., Sancho, J., Alonso, P. J., Gómez-Moreno, C., Mayoral, J. A., and Martínez, J. I. (2002) *J. Phys. Chem. A* **106**, 4729–4735
- Kay, C. W. M., Schleicher, E., Hitomi, K., Todo, T., Bittl, R., and Weber, S. (2005) *Magn. Reson. Chem.* **43**, S96–S102
- Park, H.-W., Kim, S.-T., Sancar, A., and Deisenhofer, J. (1995) *Science* **268**, 1866–1872
- Williams-Smith, D. L., Bray, R. C., Barber, M. J., Tsopanakis, A. D., and Vincent, S. P. (1977) *Biochem. J.* **167**, 593–600
- Knauer, B. R., and Napier, J. J. (1976) *J. Am. Chem. Soc.* **98**, 4395–4400
- Khramitsov, V. V., Weiner, L. M., Grigoriev, I. A., and Volodarsky, L. B. (1982) *Chem. Phys. Lett.* **91**, 69–72
- Schwartz, R. N., Peric, M., Smith, S. A., and Balcs, B. L. (1997) *J. Phys. Chem. B* **101**, 8735–8739
- Saracino, G. A. A., Tedeschi, A., D'Errico, G., Improta, R., Franco, L., Ruzzi, M., Corvaia, C., and Barone, V. (2002) *J. Phys. Chem. A* **106**, 10700–10706
- Mees, A., Klar, T., Gnau, P., Hennecke, U., Eker, A. P. M., Carell, T., and Essen, L.-O. (2004) *Science* **306**, 1789–1793
- Kim, J.-K., and Choi, B.-S. (1995) *Fur. J. Biochem.* **228**, 849–854
- Kim, J.-K., Patel, D., and Choi, B.-S. (1995) *Photochem. Photobiol.* **62**, 44–50
- Ii, J., Uchida, T., Ohta, T., Todo, T., and Kitagawa, T. (2006) *J. Phys. Chem. B* **110**, 16724–16732

Autonomic and cardiovascular responses to scent stimulation are altered in cry KO mice

Mamoru Tanida^{a,*}, Atsushi Yamatodani^b, Akira Niijima^c, Jiao Shen^a,
Takeshi Todo^d, Katsuya Nagai^a

^a Institute for Protein Research, Osaka University, 3-2 Yamada-Oka, Suita, Osaka 565-0871, Japan

^b Graduate School of Medicine, Osaka University, 1-7 Yamada-Oka, Suita, Osaka 565-0871, Japan

^c Niigata University School of Medicine, 757 Asahimachi-Dori Ichiban-Cho, Niigata 951-8510, Japan

^d Radiation Biology Center, Kyoto University, Yoshida Konoe-Cho, Sakyo-Ku, Kyoto 606-8501, Japan

Received 2 October 2006; received in revised form 21 November 2006; accepted 26 November 2006

Abstract

Previously, we observed that in rats, olfactory stimulation with scent of grapefruit oil (SGFO) elevates the activities of sympathetic nerves. SGFO also suppresses gastric vagal (parasympathetic) nerve activity (GVNA), increases the plasma glycerol concentration, blood pressure (BP) and body temperature, and reduces appetite. In contrast, olfactory stimulation with scent of lavender oil (SLVO) has opposite effects in rats. Here, we show that in mice, olfactory stimulation with SGFO elevated activities of sympathetic nerves innervating the kidney, adrenal gland and brown adipose tissue as well as increasing BP and suppressing GVNA, whereas olfactory stimulation with SLVO decreased these sympathetic nerve activities and BP, and elevated GVNA. Electrolytic lesions of the mouse hypothalamic suprachiasmatic nucleus (SCN) eliminated changes in renal sympathetic nerve activity (RSNA), BP and GVNA induced by either SGFO or SLVO. Furthermore, SGFO-induced elevations in RSNA and BP and the SLVO-induced GVNA increase were not observed in Cryptochrome (Cry)-deficient mice, which harbor mutations in both *cry1* and *cry2* and lack normal circadian rhythms. These findings suggest that SGFO and SLVO affect autonomic neurotransmission and BP via the SCN in mice. Moreover, the molecular clock mechanism in the SCN, which involves the *cry1* and *cry2* genes, is partially involved in mediating these autonomic and cardiovascular actions of SGFO and SLVO.

© 2006 Elsevier Ireland Ltd. All rights reserved.

Keywords: Suprachiasmatic nucleus; Autonomic nerves; Cryptochrome; Blood pressure

In mammals, the hypothalamic suprachiasmatic nucleus (SCN) functions as a master circadian clock and forms circadian rhythms in physiological phenomena and behaviors [10]. Previously, we observed that the hyperglycemia induced by 2-deoxy-D-glucose (2DG) [13], an inhibitor of glucose utilization, is associated with excitations of sympathetic nerves innervating the pancreas, liver and adrenal gland, a reduction in the blood insulin level and elevations in the blood glucagon and adrenaline level [13]. Since a daily rhythm was observed in the hyperglycemia induced by 2DG [15], the effect of bilateral electrolytic lesions of the SCN was examined and it was found that these lesions eliminated the 2DG-induced hyperglycemia [13]

and autonomic changes [14]. These findings raised the possibility that the SCN is involved in the control of blood glucose via regulation of autonomic activities. Supporting this possibility, we found that pseudorabies virus (PRV), which is retrogradely and multi-synaptically transported along the neural pathway, when injected into the pancreas, was transported to the SCN via sympathetic and parasympathetic relay neurons in the central nervous system [6,7]. These findings suggest that the SCN sends autonomic projections to these peripheral organs and tissues.

Recently, we observed that olfactory stimulation with scent of grapefruit oil (SGFO) or scent of lavender oil (SLVO) affects autonomic neurotransmission and elicits changes in lipolysis, thermogenesis, food intake, body weight and blood pressure (BP) in rats [22,23,25,26]. To investigate this phenomenon, we firstly established whether the responses to SGFO and SLVO also exist in mice, and confirmed that either SGFO or SLVO causes autonomic and cardiovascular changes. Moreover, our previous study found that bilateral lesions of the SCN

* Corresponding author at: Y.M.P.-International Corporation, 4th Floor, Nakajima-Building, 4-12-17 Toyosaki, Kita-Ku, Osaka 531-0072, Japan.
Tel.: +81 6 6486 1080; fax: +81 6 6486 1081.

E-mail address: mtanida@ymp-i.co.jp (M. Tanida).

eliminated these SGFO- and SLVO-induced changes in rats [25,26]. These facts raised a possibility that the molecular mechanism of circadian clock in the SCN is involved in the regulation of autonomic nerves, thus in those of physiological phenomena. To examine whether the molecular mechanism in the SCN [10] is responsible for the control of autonomic nervous system, we determined whether the above responses to SGFO and SLVO were observed in *Cry1* and *2* double knockout [*Cry(-/-)*] mice, which lack circadian rhythm in their locomotion under constant dark conditions [29].

Sixteen to eighteen week old male C3H mice (wild-type mice, $n = 130$) and *cry1* and *cry2* mutant mice (*Cry(-/-)*, $n = 29$) [29] backcrossed in C3H background were used. Animals were housed in a room maintained at 24 ± 1 °C and illuminated for 12 h (07:00 to 19:00) everyday. Food and water were freely available. To record locomotor activity of animals under constant dark conditions (DD), the activity of a mouse in an individual cage was monitored using a far-infrared monitoring apparatus (Bio-Medica Co., Japan). Since light suppressed the activity of *Cry(-/-)* mice [28], electrophysiological experiments were performed in the DD. All animal care and handling procedures were approved by the Institutional Animal Care and Use Committee of the Institute for Protein Research, Osaka University.

General preparations were performed as described previously [25]. Briefly, under anesthesia [1 g/kg urethane, intraperitoneal (i.p.)], mice cannulated intratracheally were fixed in a stereotaxic apparatus. The adequacy of the depth was checked by paw pinch [12]. For recording renal sympathetic nerve activity (RSNA) and adrenal sympathetic nerve activity (ASNA), the left renal and adrenal nerves were exposed retroperitoneally through a left flank incision. For recording brown adipose tissue sympathetic nerve activity (BAT-SNA), the left BAT nerve was dissected from ventral surface of the left interscapular BAT pad. For recording gastric vagal nerve activity (GVNA), the gastric branch of the ventral subdiaphragmatic vagal nerve was identified and exposed on the esophagus after incision of the abdomen midline [18]. The distal end of the respective nerve was ligated, and then hooked up with a pair of silver wire electrodes for recording efferent nerve activity. Electrical changes in neural activities were recorded and analyzed as described previously [25]. Mean arterial pressure (MAP) was calculated from the BP data sampled in off-line analysis. For olfactory stimulation, grapefruit essential oil (*Citrus Paradisii*, Pranarom International, Belgium) and lavender essential oil (*Lavendula angustifolia*, Pranarom International, Belgium) were suspended in a 100-fold volume of water. A cubic cotton gauze, soaked in the suspension, was placed on the bottom of a plastic tube and the mouse's nose was placed inside the plastic tube for 10 min. At the end of the experiment, hexamethonium chloride (10 mg/kg) was intravenously administered to block evoked potentials in order to determine the noise level of the recording.

In some mice ($n = 35$), about 3 weeks prior to olfactory stimulation, bilateral electrolytic lesions of the SCN were performed. Briefly, under pentobarbital anesthesia (35 mg/kg, i.p.), a stainless steel electrode was inserted into the SCN using coordinates A-P, 0.2 mm posterior to bregma; L, 0 mm from the midline; V, 7.0 mm from the skull surface [20], following which a 0.5-mA

anodal direct current was passed through the electrode for 10 s. Control mice received a sham operation without the current. At the end of the experiment, the brain was removed and histologically examined to verify placement of bilateral lesions in the SCN by Cresyl violet staining.

The RSNA, MAP, GVNA and BAT-SNA measured during each 5 min period after olfactory stimulations were evaluated by digital signal processing and statistical analyses. All data were expressed as means \pm S.E.M. Normality in the data or differences in respective basal values (0 min) were detected by Kolmogorov–Smirnov test or Mann–Whitney *U*-test, respectively. Because of the inter-individual variability in the pre-injection state, percent change was calculated for RSNA, MAP, GVNA, ASNA and BAT-SNA. Two-way analysis of variance (ANOVA) was applied to compare group responses to olfactory stimulations. $P < 0.05$ was applied as significant level.

Typical recording data of the RSNA, blood pressure, GVNA, ASNA and BAT-SNA before and after olfactory stimulation with SGFO or SLVO are shown in Fig. 1. Control treatment using water without oils did not affect autonomic neurotransmission. In contrast, olfactory stimulation with SGFO increased renal sympathetic nerve activity (RSNA), adrenal sympathetic nerve activity (ASNA), brown adipose tissue-sympathetic nerve activity (BAT-SNA) and BP, and decreased gastric vagal nerve activity (GVNA) in mice (Fig. 1A). Moreover, SLVO lowered RSNA, ASNA, BAT-SNA and BP, and elevated GVNA (Fig. 1A). Significance of differences for periods between 5 and 75 min after olfactory stimulation with SGFO and water were compared by ANOVA and results were as follows: RSNA, $P < 0.001$ ($F = 30$); MAP, $P < 0.001$ ($F = 25$); ASNA, $P < 0.001$ ($F = 38$); BAT-SNA, $P < 0.001$ ($F = 34$); GVNA, $P < 0.005$ ($F = 60$) (Fig. 1B–F). Comparison of similar parameters in water and SLVO-exposed groups by ANOVA produced the following results: RSNA, $P < 0.001$ ($F = 93$); MAP, $P < 0.001$ ($F = 35$); ASNA, $P < 0.001$ ($F = 34$); BAT-SNA, $P < 0.001$ ($F = 26$); GVNA, $P < 0.001$ ($F = 40$) (Fig. 1B–F). Absolute basal (0 min) values of these parameters for the experiments shown in Fig. 1 are summarized in Table 1; none of the basal values differed significantly between SGFO-exposed, SLVO-exposed and water-exposed groups, according to the Mann–Whitney *U*-test.

We examined the effects of bilateral lesions of the SCN in mice. As expected, SCN lesions also abolished these responses to SGFO and SLVO in mice (Fig. 2). Although part of the optic chiasm was damaged in some SCN-lesioned mice (Fig. 2A), pupillary reflexes induced by light stimulation to both eyes were intact in all mice. In sham-operated mice, RSNA and MAP (Fig. 2B and C) were elevated and GVNA (Fig. 2D) was suppressed by SGFO, and RSNA and MAP were lowered and GVNA was enhanced by SLVO. In contrast, in SCN-lesioned mice, SGFO and SLVO did not affect RSNA (Fig. 2B), MAP (Fig. 2C) or GVNA (Fig. 2D). Thus, bilateral lesions of the SCN eliminated all changes in RSNA, MAP and GVNA induced by olfactory stimulations with either SGFO or SLVO. Absolute basal (0 min) RSNA, MAP and GVNA values for the experiments shown in Fig. 2 are summarized in Table 1; basal values

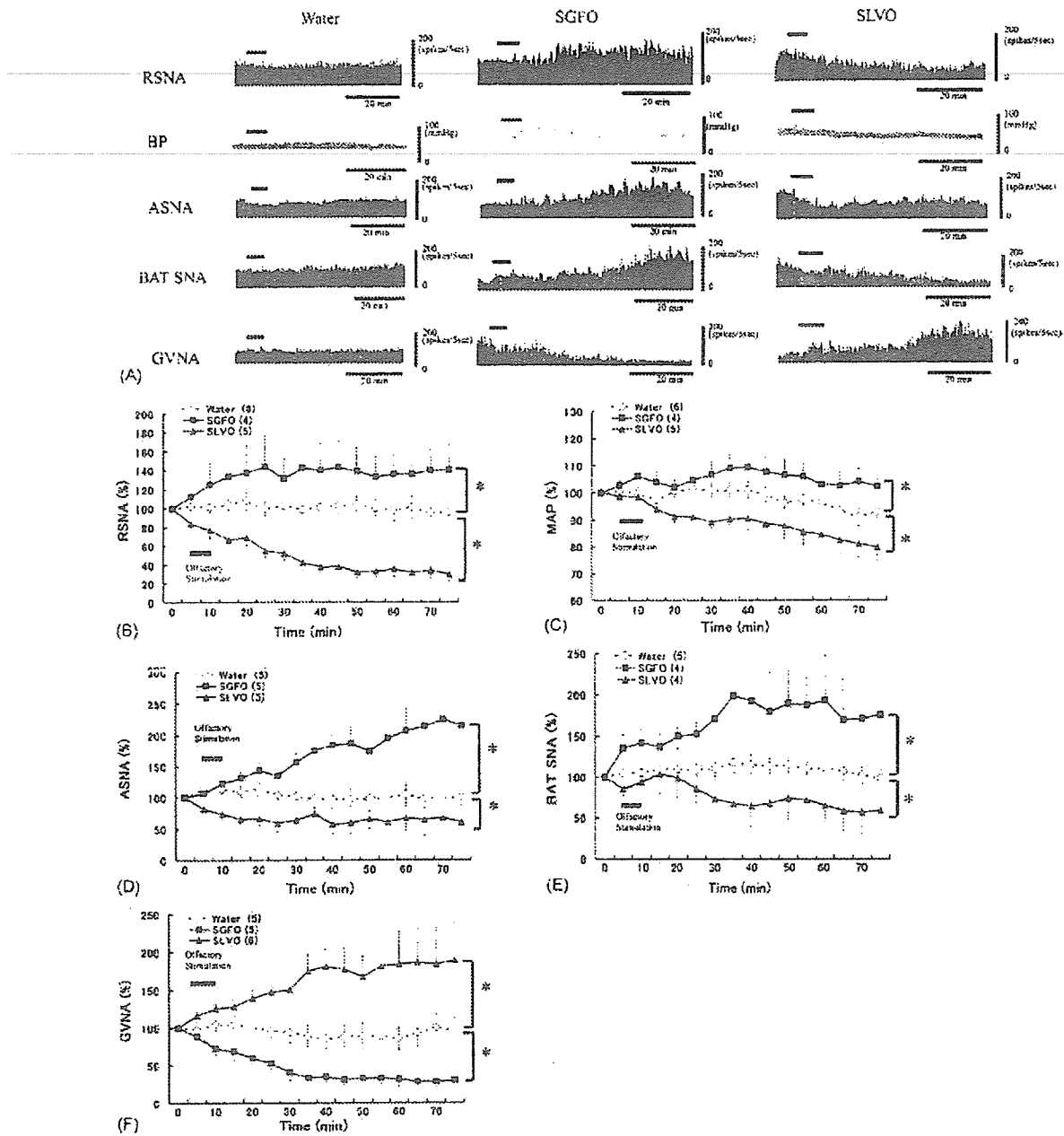


Fig. 1. Effects of olfactory stimulation with SGFO or SLVO on autonomic neurotransmission and BP. (A) Representative recordings of nerve activities and BP stimulated with water, SGFO or SLVO. Upper bars indicate the 10-min stimulation period. Changes in RSNA (B), MAP (C), ASNA (D), BAT-SNA (E) and GVNA (F) after olfactory stimulation are expressed as means \pm S.E. of the percentages 0 min values. Numbers of animals are shown in the parentheses. * $P < 0.05$ vs. water.

did not differ significantly between water, SGFO or SLVO groups, as determined by Mann–Whitney *U*-test.

To examine whether the molecular mechanism in the SCN [10] is responsible for the control of autonomic nervous system and thus is involved in mediating the effects of SGFO and SLVO, we determined whether the above responses to SGFO and SLVO were observed in *Cry1* and *2* double knockout [*Cry(-/-)*] mice, which lack circadian rhythm in their locomotion under constant dark conditions (Fig. 3A). Similar to the effects in rats, in wild-type mice, SGFO elevated RSNA and MAP (Fig. 3B and C) and suppressed GVNA (Fig. 3D) while SLVO lowered RSNA and MAP and enhanced GVNA. However, most of these effects were

eliminated in *Cry(-/-)* mice. The suppression effects of SLVO on RSNA and MAP and activation effect of SLVO on GVNA were maintained in *Cry(-/-)* mice. Thus, mutations of *cry1* and *cry2* genes largely suppressed elevations in RSNA, MAP and GVNA induced by olfactory stimulations with SGFO and SLVO, respectively. Absolute basal (0 min) RSNA, MAP and GVNA values for these experiments shown in Fig. 3 are summarized in Table 1; basal values did not differ significantly between groups, as determined by Mann–Whitney *U*-test. These findings suggest that these clock-related gene products may be involved in mediating autonomic neurotransmission and cardiovascular responses to olfactory stimulation.

Table 1
Basal levels (0 min) in experimental group

Groups	RSNA (spikes/5 s) (n)	MAP (mmHg) (n)	GVNA (spikes/s) (n)	ASNA (spikes/s) (n)	BAT-SNA (spikes/s) (n)
Experiment (1)					
Water	123.1 ± 45.2 (6)	60.1 ± 4.6 (6)	91.5 ± 24.6 (5)	148.0 ± 54.0 (5)	141.4 ± 29.4 (5)
SGFO	111.6 ± 11.5 (4)	58.7 ± 4.3 (4)	108.9 ± 19.1 (5)	182.2 ± 12.1 (5)	75.8 ± 14.3 (5)
SLVO	76.4 ± 9.0 (5)	55.5 ± 7.1 (5)	132.7 ± 31.9 (6)	126.6 ± 21.9 (5)	132.9 ± 17.3 (4)
Experiment (2)					
SCN-sham, SGFO	116.2 ± 17.6 (4)	61.5 ± 2.1 (4)	91.2 ± 31.0 (3)		
SCN-sham, SLVO	147.5 ± 23.4 (3)	63.1 ± 3.8 (3)	89.5 ± 13.4 (4)		
SCN-lesion, SGFO	104.6 ± 18.3 (6)	59.1 ± 5.9 (3)	120.3 ± 19.4 (3)		
SCN-lesion, SLVO	109.8 ± 30.2 (3)	62.4 ± 10.2 (3)	136.9 ± 25.8 (3)		
Experiment (3)					
Wild, SGFO	93.2 ± 20.5 (4)	61.8 ± 5.3 (4)	99.6 ± 20.4 (4)		
Wild, SLVO	110.2 ± 27.2 (4)	65.9 ± 8.8 (4)	85.8 ± 5.4 (4)		
DKO, SGFO	89.4 ± 9.0 (4)	61.2 ± 6.9 (4)	80.6 ± 38.2 (4)		
DKO, SLVO	178.4 ± 63.1 (3)	58.4 ± 9.5 (3)	69.4 ± 13.9 (4)		

Wild, wild-type mice; DKO, Cry(−/−) mice. Data are presented as means ± S.E.M.

Since excitation of sympathetic nerve activity is closely related to a reduction in body weight [5], we examined body weights and a portion of the visceral adipose tissues (mesenteric + perirenal + epididymal adipose tissues). Notably, significant reductions in both of these parameters were observed in Cry(−/−) mice [wild versus Cry(−/−): 31.9 ± 1.8 g (*n* = 24) versus 22.0 ± 0.6 g (*n* = 23) for body weight (*P* < 0.05 by Mann–Whitney *U*-test); 1.8 ± 0.2 g (*n* = 24) versus 0.4 ± 0.1 g (*n* = 23) for adipose tissue weight (*P* < 0.05 by Mann–Whitney *U*-test)].

In this study, we observed that in mice, SGFO and SLVO affected RSNA, ASNA, BAT-SNA, BP and GVNA in a manner similar to that observed in rats [22,23,25,26]. In rats, anosmic treatments with ZnSO₄ or xylocaine abolished these responses [22,23,25,26] thus it is likely that in mice, responses to SGFO

and SLVO might also be elicited through olfactory receptors in the nasal mucosa. SGFO- and SLVO-induced changes in RSNA, GVNA and BP were eliminated by bilateral electrolytic lesions of the SCN in mice (Fig. 2), as was previously observed in rats [25,26]. These findings also suggest that the SCN, a master circadian oscillator, might be involved in autonomic and cardiovascular changes due to SGFO and SLVO in mice.

Thus, we verified whether the effects of SGFO and SLVO were altered in Cry(−/−) mice, who lack normal circadian locomotor activity. As expected, we observed that SGFO-induced elevations of RSNA and BP did not occur, and SLVO-induced elevation of GVNA was largely suppressed in Cry(−/−) mice, suggesting that Cry 1 and 2 in the SCN might be, at least partially, implicated in these physiological effects of SGFO and SLVO. Moreover, we preliminarily

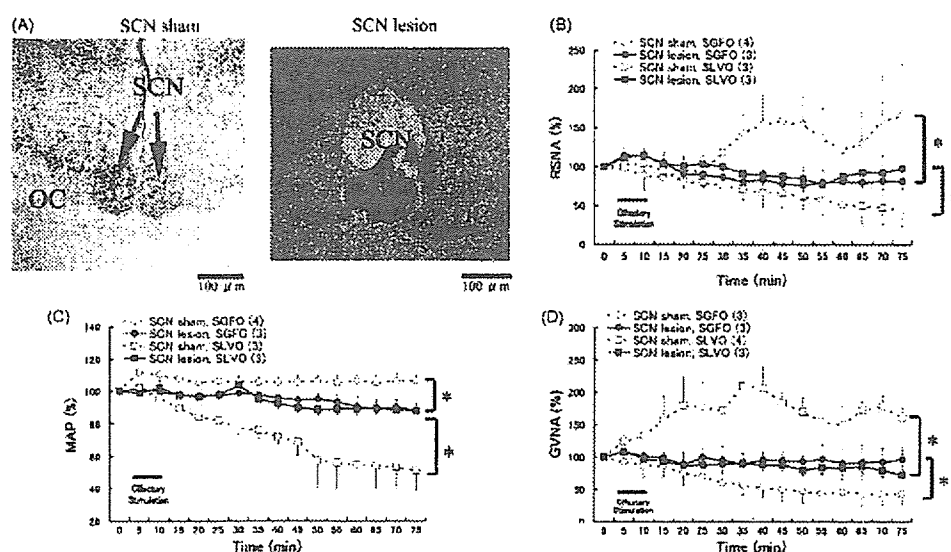


Fig. 2. Effects of lesion of the SCN on SGFO- or SLVO-induced changes in autonomic neurotransmission and BP. (A) Photomicrographs of representative coronal brain sections including the SCN of a sham-operated (SCN sham) and an SCN-lesioned (SCN lesion) mouse. OC, optic chiasm. (B), MAP (C) and GVNA (D) after olfactory stimulation are expressed as means ± S.E. of the percentages 0 min values. **P* < 0.05 vs. SCN sham.

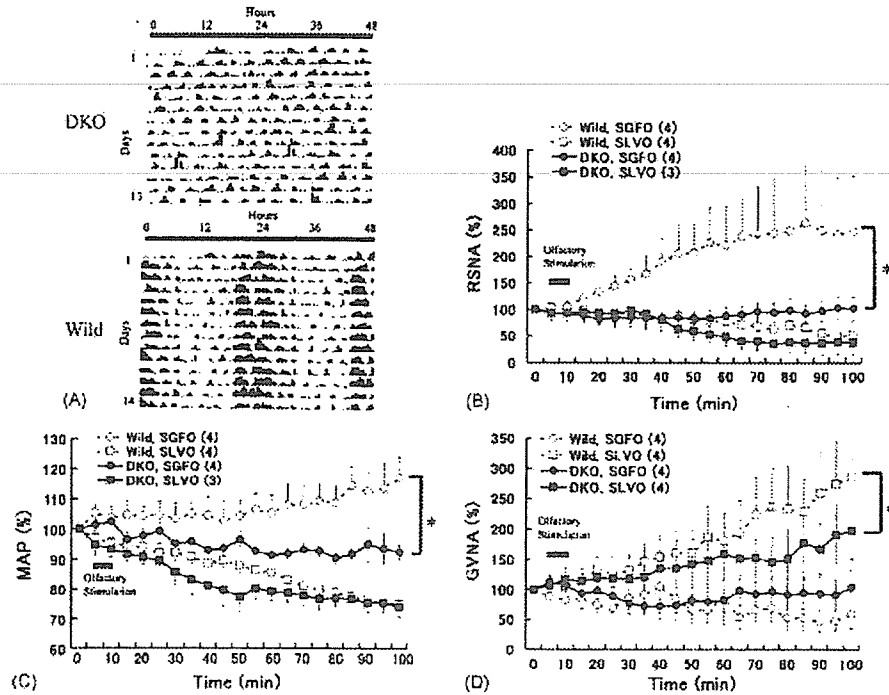


Fig. 3. Effects of olfactory stimulation with SGFO or SLVO on autonomic neurotransmission and BP in wild-type and *Cry(-/-)* mice. (A) Representative locomotor activity of wild-type (wild) and *Cry(-/-)* (DKO) mice under constant dark conditions are presented as a double plot. RSNA (B), MAP (C) and GVNA (D) after olfactory stimulation are expressed as means \pm S.E. of the percentages 0 min values. * $P < 0.05$ vs. wild.

examined blood levels of noradrenaline and adrenaline in addition to glucose to identify body condition status. Under urethane anesthesia (1 g/kg, i.p.), blood samples (0.2 ml each) were withdrawn from the abdominal artery, and adrenaline and noradrenaline in the deproteinized plasma were determined in a fully automated HPLC-fluorometric system (Model HLC-725CA Catecholamine Analyzer, Tosoh, Japan) using a diphenylethylenediamine condensation method [19]. The plasma glucose levels were measured with a Fuji Dri-chem system (Fuji Film, Japan). The blood levels of adrenaline (pmol/ml), noradrenaline (pmol/ml) and glucose (mg/dl) of wild-type mice were 1.02 ± 0.19 ($n=3$), 6.67 ± 1.26 ($n=4$) and 195.7 ± 14.9 ($n=4$), respectively, whereas that of *Cry(-/-)* mice were 1.24 ± 0.43 ($n=3$), 6.26 ± 1.42 ($n=4$) and 254.3 ± 15.3 ($n=4$), respectively. Therefore, the adrenaline and glucose levels were significantly higher in *Cry(-/-)* mice than in wild-type mice ($P < 0.05$, by Mann-Whitney *U*-test). These data suggest a possibility that the hyperglycemic and hyperadrenalinemic state might exist in *Cry(-/-)* mice. Moreover, using immunohistochemical method, we preliminarily examined changes in the expression of *c-Fos* protein in the hypothalamic paraventricular nucleus (PVN) and SCN as a marker of neural transmission. Mean numbers of *c-Fos* expression in the PVN and SCN of wild-type mice were 100.9 ± 28.1 ($n=3$) and 109.0 ± 37.8 ($n=3$), respectively, whereas that of *Cry(-/-)* mice were 181.1 ± 44.9 ($n=3$) and 293.1 ± 79.7 ($n=3$), respectively, and these values are different between wild-type and *Cry(-/-)* mice ($P < 0.05$, by Mann-Whitney *U*-test). In studying with the PRV we found evidence that autonomic projections from the SCN to the pancreas, liver and adrenal gland passed through the PVN [6,7].

Therefore, the stimulation in the PVN might be secondary to that of the SCN.

Considering that BP and body temperature [11,16] were higher, and weights of body and adipose tissues were lower in *Cry(-/-)* mice, it seems that sympathetic nerves, which innervate the adrenal gland and BAT, controlling adrenaline release and thermogenesis, respectively, might be activated via a mechanism involving neural excitation of the SCN and PVN. Thus, it is possible that already elevated sympathetic tone originated from the SCN in *Cry(-/-)* mice might cause the deterioration in the autonomic and cardiovascular responses to SGFO and SLVO (Fig. 3). In this regard, it has been reported that obesity associated with hypertriglyceridemia, hypercholesterolemia and hyperglycemia is observed in Clock mutant mice [27]. Therefore, it is quite likely that the molecular circadian clock mechanism in the SCN is involved in the homeostasis of glucose and lipid metabolism, food intake, BP and body temperature through regulation of autonomic neurotransmission. With regard to the role of the SCN, it has previously been suggested that the SCN sends sympathetic and parasympathetic neural inputs to peripheral organs and tissues [2,3,6–9,24]. We obtained evidence that the originating SCN neurons of the sympathetic and parasympathetic neural connections to the periphery are different [7]. Therefore, it might be possible that in *Cry(-/-)* mice, activities of respective original neurons of the sympathetic and parasympathetic nerves were both in exciting conditions, causing the conditions favor to sympathetic excitations in peripheral organs and tissues. Thus, in *Cry(-/-)* mice, effects of sympathetic excitations in them might be dominant compared with those of parasympathetic excitations. This might cause the

suppressions of further excitations but not inhibitions in the sympathetic original and parasympathetic original neurons in the SCN due to SGFO and SLVO and thus largely suppress the elevating responses of RSNA and GVNA due to SGFO and SLVO (Fig. 3). Whether these are the cases must be examined in future.

These defects in autonomic neurotransmissions observed in mice lacking the intact molecular clock mechanism might be related with the mechanism of depressive state in patients with winter depression, which is regarded as a disease caused by the circadian clock disturbance and is known to have lower odor detection thresholds [21] and abnormality of autonomic functions [1], because the response of autonomic nerve activities is suggested to be implicated in the formation of emotions [4]. On the other hand, Nievergelt et al. found that there was not close association bipolar disease with Cry 1 gene [17]. However, lacking both genes of Cry 1 and Cry 2 caused loss of the circadian rhythm, and lacking of Cry1 gene maintains the circadian rhythm [29]. Therefore, whether there is connection between bipolar disease and Cry1 and Cry2 remained to be studied.

In conclusion, the results obtained here suggest that the molecular circadian clock mechanism is, at least partly, involved in mediating the elevating effects of SGFO and SLVO on autonomic and cardiovascular functions.

References

- [1] M.L. Austen, G.V. Wilson, Increased vagal tone during winter in subsyndromal seasonal affective disorder, *Biol. Psychiatry* 50 (2001) 28–34.
- [2] M. Bamshad, C.K. Song, T.J. Bartmess, CNS origins of the sympathetic nervous system outflow to brown adipose tissue, *Am. J. Physiol.* 276 (1999) R1569–R1578.
- [3] T.J. Bartmess, M. Bamshad, Innervation of mammalian white adipose tissue: implications for the regulation of total body fat, *Am. J. Physiol.* 275 (1998) R1399–R1411.
- [4] M.F. Bear, B.W. Connors, M.A. Paradiso, *Neuroscience, Exploring the Brain*, second ed., Lippincott, Baltimore MD, 1996, p. 855.
- [5] G. Bray, D. York, The MONALISA hypothesis in the time of leptin, *Recent Progr. Horm. Res.* 53 (1998) 94–118.
- [6] R.M. Buijs, S. Chun, A. Nijijima, H.J. Romijn, K. Nagai, Parasympathetic and sympathetic control of the pancreas: a role for the suprachiasmatic nucleus and other hypothalamic centers that are involved in the regulation of food intake, *J. Comp. Neurol.* 431 (2001) 405–423.
- [7] R.M. Buijs, S.I. Fleur, J. Wortel, C.V. Heynigen, L. Zuiddam, T.C. Mettenleiter, A. Kalsbeek, K. Nagai, A. Nijijima, The suprachiasmatic nucleus balances sympathetic and parasympathetic output to peripheral organs through separate preautonomic neurons, *J. Comp. Neurol.* 464 (2003) 36–48.
- [8] R.M. Buijs, J. Wortel, J.J. Van Heerikhuizen, M.G. Feenstra, G.J. Ter Horst, H.J. Romijn, A. Kalsbeek, Anatomical and functional demonstration of a multisynaptic suprachiasmatic nucleus adrenal (cortex) pathway, *Eur. J. Neurosci.* 11 (1999) 1544–1595.
- [9] S.E. le Fleur, A. Kalsbeek, J. Wortel, R.M. Buijs, Polysynaptic neural pathways between the hypothalamus, including the suprachiasmatic nucleus and the liver, *Brain Res.* 871 (2000) 50–56.
- [10] P.L. Lowry, J.S. Takahashi, Mammalian circadian biology: elucidating genome-wide levels of temporal organization, *Ann. Rev. Genomics Hum. Genet.* 5 (2004) 407–441.
- [11] S. Masuki, T. Todo, Y. Nakano, H. Okamura, H. Nose, Reduced alpha-adrenoceptor responsiveness and enhanced baroreflex sensitivity in Cry-deficient mice lacking a biological clock, *J. Physiol.* 566 (2005) 213–224.
- [12] T. Mutoh, A.C. Bonham, J.P. Joad, Substance P in the nucleus of the solitary tract augments bronchopulmonary C fiber reflex output, *Am. J. Physiol.* 279 (2000) R1215–R1223.
- [13] K. Nagai, N. Nagai, K. Shimizu, S. Chun, H. Nakagawa, A. Nijijima, SCN output drives the autonomic nervous system: with special reference to the autonomic function related to the regulation of glucose metabolism, *Prog. Brain Res.* 111 (1996) 253–272.
- [14] K. Nagai, A. Nijijima, N. Nagai, H. Hibino, S. Chun, K. Shimizu, H. Nakagawa, Bilateral lesions of the hypothalamic suprachiasmatic nucleus eliminated sympathetic response to intracranial injection of 2-deoxy-D-glucose and VIP rescued this response, *Brain Res. Bull.* 39 (1996) 293–297.
- [15] K. Nagai, H. Yamamoto, H. Nakagawa, Time-dependent hyperglycemic actions of centrally administered 2-deoxy-D-glucose, D-mannitol and D-glucose, *Biomed. Res.* 3 (1982) 288–293.
- [16] K. Nagashima, K. Matsue, M. Konishi, C. Iidaka, K. Miyazaki, N. Ishida, K. Kanosue, The involvement of Cry1 and Cry2 genes in the regulation of the circadian body temperature rhythm in mice, *Am. J. Physiol.* 288 (2005) R329–R335.
- [17] C.M. Nievergelt, D.F. Kripke, R.A. Remick, A.D. Sadovnick, S.L. McElroy, P.E. Keck, J.R. Kelsoe, Examination of the clock gene Cryptochrome 1 in bipolar disorder: mutational analysis and absence of evidence for linkage or association, *Psychiatr. Genet.* 15 (2005) 45–52.
- [18] A. Nijijima, Effect of umami taste stimulations on vagal efferent activity in the rat, *Brain Res. Bull.* 27 (1991) 393–396.
- [19] H. Nohta, A. Mitsui, Y. Ohkura, Spectrofluorimetric determination of catecholamines with 1,2-diphenylethylenediamine, *Anal. Chim. Acta* 165 (1984) 171–176.
- [20] G. Paxinos, C. Watson, *The Rat Brain in Stereotaxic Coordinates*, fourth ed., Academic Press, Sydney, 1998.
- [21] T.T. Postolache, T.A. Wehr, R.L. Doty, L. Sher, E.H. Turner, J.J. Bartko, N.E. Rosenthal, Patients with seasonal affective disorder have lower odor detection thresholds than control subjects, *Arch. Gen. Psychiatry* 59 (2002) 1119–1122.
- [22] J. Shen, A. Nijijima, M. Tanida, Y. Horii, K. Maeda, K. Nagai, Olfactory stimulation with scent of grapefruit oil affects autonomic nerves, lipolysis and appetite in rats, *Neurosci. Lett.* 380 (2005) 289–294.
- [23] J. Shen, A. Nijijima, M. Tanida, Y. Horii, K. Maeda, K. Nagai, Olfactory stimulation with scent of lavender oil affects autonomic nerves, lipolysis and appetite in rats, *Neurosci. Lett.* 383 (2005) 188–193.
- [24] J.D. Sly, L. Colvill, J.M. McKinley, J.B. Oldfield, Identification of neural projections from the forebrain to the kidney using the virus pseudorabies, *J. Auton. Nerv. Syst.* 77 (1999) 73–82.
- [25] M. Tanida, A. Nijijima, J. Shen, T. Nakamura, K. Nagai, Olfactory stimulation with scent of essential oil of grapefruit affects autonomic neurotransmission and blood pressure, *Brain Res.* 1058 (2005) 44–55.
- [26] M. Tanida, A. Nijijima, J. Shen, T. Nakamura, K. Nagai, Olfactory stimulation with scent of lavender oil affects autonomic neurotransmission and blood pressure in rats, *Neurosci. Lett.* 398 (2006) 155–160.
- [27] F.W. Turek, C. Joshi, A. Kohsaka, E. Lin, G. Ivanova, E. McDearmon, A. Laposky, S. Losee-Olson, A. Easton, D.R. Jensen, R.H. Eckel, J.S. Takahashi, J. Bass, Obesity and metabolic syndrome in circadian clock mutant mice, *Science* 308 (2005) 1043–1045.
- [28] G.T. van der Horst, M. Muijtjens, K. Kobayashi, R. Takano, S. Kanno, M. Takao, J. de Wit, A. Verkerk, A.P. Eker, D. van Leenen, R. Buijs, D. Bootsma, J.H. Hoeijmakers, A. Yasui, Mammalian Cry1 and Cry2 are essential for maintenance of circadian rhythms, *Nature* 398 (1999) 627–630.
- [29] M.H. Vitaterna, C.P. Selby, T. Todo, H. Niwa, C. Thompson, E.M. Fruechte, K. Hitomi, R.J. Thresher, T. Ishikawa, J. Miyazaki, J.S. Takahashi, A. Sancar, Differential regulation of mammalian period genes and circadian rhythmicity by cryptochromes 1 and 2, *Proc. Natl. Acad. Sci. U.S.A.* 96 (1999) 12114–12119.

Menstrual Blood-derived Cells Confer Human Dystrophin Expression in the Murine Model of Duchenne Muscular Dystrophy via Cell Fusion and Myogenic Transdifferentiation

ChangHao Cui,^{*†} Taro Uyama,^{*} Kenji Miyado,^{*} Masanori Terai,^{*} Satoru Kyo,[‡] Tohru Kiyono,[§] and Akihiro Umezawa^{*}

^{*}Department of Reproductive Biology and Pathology, National Institute for Child Health and Development, Tokyo, 157-8567, Japan; [†]Department of Basic Medical Science, Mudanjiang Medical College, Mudanjiang, 157011, China; [‡]Department of Obstetrics and Gynecology, Kanazawa University, School of Medicine, Kanazawa, 920-8640, Japan; and [§]Virology Division, National Cancer Center Research Institute, Tokyo, 104-0045, Japan

Submitted September 28, 2006; Revised January 19, 2007; Accepted February 6, 2007
Monitoring Editor: M. Bishr Omary

Duchenne muscular dystrophy (DMD), the most common lethal genetic disorder in children, is an X-linked recessive muscle disease characterized by the absence of dystrophin at the sarcolemma of muscle fibers. We examined a putative endometrial progenitor obtained from endometrial tissue samples to determine whether these cells repair muscular degeneration in a murine mdx model of DMD. Implanted cells conferred human dystrophin in degenerated muscle of immunodeficient mdx mice. We then examined menstrual blood-derived cells to determine whether primarily cultured nontransformed cells also repair dystrophied muscle. In vivo transfer of menstrual blood-derived cells into dystrophic muscles of immunodeficient mdx mice restored sarcolemmal expression of dystrophin. Labeling of implanted cells with EGFP and differential staining of human and murine nuclei suggest that human dystrophin expression is due to cell fusion between host myocytes and implanted cells. In vitro analysis revealed that endometrial progenitor cells and menstrual blood-derived cells can efficiently transdifferentiate into myoblasts/myocytes, fuse to C2C12 murine myoblasts by in vitro coculturing, and start to express dystrophin after fusion. These results demonstrate that the endometrial progenitor cells and menstrual blood-derived cells can transfer dystrophin into dystrophied myocytes at a high frequency through cell fusion and transdifferentiation in vitro and in vivo.

AQ:1

INTRODUCTION

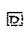
Skeletal muscle consists predominantly of syncytial fibers with peripheral, postmitotic myonuclei, and its intrinsic repair potential in adulthood relies on the persistence of a resident reserve population of undifferentiated mononuclear cells, termed “satellite cells.” In mature skeletal muscle, most satellite cells are quiescent and are activated in response to environmental cues, such as injury, to mediate postnatal muscle regeneration. After division, satellite cell progeny, termed myoblasts, undergo terminal differentiation and become incorporated into muscle fibers (Bischoff, 1994). Myogenesis is regulated by a family of myogenic transcription factors including MyoD, Myf5, myogenin, and MRF4 (Sabourin and Rudnicki, 2000). During embryonic development, MyoD and Myf5 are involved in the establishment of the skeletal muscle lineage (Rudnicki *et al.*, 1993), whereas myogenin is required for terminal differentiation (Hasty *et al.*, 1993; Nabeshima *et al.*, 1993). During muscle

repair, satellite cells recapitulate the expression program of the myogenic genes manifested during embryonic development.

Dystrophin is associated with a large oligomeric complex of glycoproteins that provide linkage to the extracellular membrane (Ervasti and Campbell, 1991). In Duchenne muscular dystrophy (DMD), the absence of dystrophin results in destabilization of the extracellular membrane-sarcolemma-cytoskeleton architecture, making muscle fibers susceptible to contraction-associated mechanical stress and degeneration. In the first phase of the disease, new muscle fibers are formed by satellite cells. After depletion of the satellite cell pool in childhood, skeletal muscles degenerate progressively and irreversibly and are replaced by fibrotic tissue (Cossu and Mavilio, 2000). Like DMD patients, the mdx mouse lacks dystrophin in skeletal muscle fibers (Hoffman *et al.*, 1987; Sicinski *et al.*, 1989). However, the mdx mouse develops only a mild dystrophic phenotype, probably because muscle regeneration by satellite cells is efficient for most of the animal’s life span (Cossu and Mavilio, 2000).

Myoblasts represent the natural first choice in cellular therapeutics for skeletal muscle because of their intrinsic myogenic commitment (Grounds *et al.*, 2002). However, myoblasts recovered from muscular biopsies are poorly expandable in vitro and rapidly undergo senescence (Cossu and Mavilio, 2000). An alternative source of muscle progenitor cells is therefore desirable. Cells with a myogenic potential are present in many tissues, and these cells readily

This article was published online ahead of print in *MBC in Press* (<http://www.molbiolcell.org/cgi/doi/10.1091/mbc.E06-09-0872>) on February 21, 2007.

 The online version of this article contains supplemental material at *MBC Online* (<http://www.molbiolcell.org>).

Address correspondence to: Akihiro Umezawa (omezawa@1985.jukuin.keio.ac.jp).

C. Cui *et al.*

form skeletal muscle in culture (Gerhart *et al.*, 2001). We report here that human dystrophin expression in the mdx model of DMD is attributed to cell fusion of mdx myocytes with human menstrual blood-derived stromal cells.

MATERIALS AND METHODS

Isolation of Human Endometrial Cells from Menstrual Blood

Menstrual blood samples ($n = 21$) were collected in DMEM with antibiotics (final concentrations: 100 U/ml penicillin/streptomycin) and 2% fetal bovine serum (FBS), and processed within 24 h. Ethical approval for tissue collection was granted by the Institutional Review Board of the National Research Institute for Child Health and Development, Japan. The centrifuged pellets containing endometrium-derived cells were resuspended in high-glucose DMEM medium (10% FBS, penicillin/streptomycin), maintained at 37°C in a humidified atmosphere containing 5% CO₂, and allowed to attach for 48 h. Nonadherent cells were removed by changing the medium. When the culture reached subconfluence, the cells were harvested with 0.25% trypsin and 1 mM EDTA and plated to new dishes. After 2–3 passages, the attached endometrial stromal cells were devoid of blood cells. Human EM-E6/E7/hTERT-2 cells, endometrium-derived progenitors, were obtained from surgical endometrial tissue samples and were immortalized by E6, E7, and hTERT-2 (Kyo *et al.*, 2003). C2C12 myoblast cells were supplied by RIKEN Cell Bank (The Institute of Physical and Chemical Research, Japan).

Flow Cytometric Analysis

Flow cytometric analysis was performed as previously described (Terai *et al.*, 2005). Cells were incubated with primary antibodies or isotype-matched control antibodies, followed by additional treatment with the immunofluorescent secondary antibodies. Cells were analyzed on an EPICS ALTRA analyzer (Beckman Coulter, Fullerton, CA). Antibodies against human CD13, CD14, CD29, CD31, CD34, CD44, CD45, CD50, CD54, CD55, CD59, CD73, CD90, CD105, CD117 (c-kit), CD133, HLA-ABC, and HLA-DR were purchased from Beckman Coulter, Immunotech (Marseille, France), Cytotech (Hellebaek, Denmark), and BD Biosciences Pharmingen (San Diego, CA).

In Vitro Lentivirus-mediated Gene (EGFP) Transfer into EM-E6/E7/hTERT-2 Cells

Infection of EM-E6/E7/hTERT-2 cells with lentivirus having a CMV promoter and EGFP reporter resulted in high levels of EGFP expression in all cells. Cells were analyzed for EGFP expression by flow cytometry (Miyoshi *et al.*, 1997, 1998).

In Vitro Myogenesis

Menstrual blood-derived cells or EM-E6/E7/hTERT-2 cells were seeded onto collagen I-coated cell culture dishes (Biocoat, BD Biosciences, Bedford, MA) at a density of 1×10^4 /ml in growth medium (DMEM, supplemented with 20% FBS). Forty-eight hours after seeding onto collagen I-coated dishes, cells were treated with 5-azacytidine for 24 h. Cell cultures were then washed twice with PBS and maintained in differentiation medium (DMEM, supplemented with either 2% horse serum (HS) or 1% insulin-transferrin-selenium supplement [ITS]). The differentiation medium was changed twice a week until the experiment was terminated.

RT-PCR Analysis of EM-E6/E7/hTERT-2 Cells and Menstrual Blood-derived Cells

Total RNA was prepared using Isogen (Nippon Gene, Tokyo, Japan). Human skeletal muscle RNA was purchased from TOYOBO (Osaka, Japan). RT-PCR of Myf5, MyoD, desmin, myogenin, myosin heavy chain- β /d (MyHC- β /d), and dystrophin was performed with 2 μ g of total RNA. RNA for RT-PCR was converted to cDNA with a first-stand cDNA synthesis kit (Amersham Pharmacia Biotechnology, Piscataway, NJ) according to the manufacturer's recommendations. The sequences of PCR primers that amplify human but not mouse genes are listed in Supplementary Table 1. PCR was performed with TaKaRa recombinant Taq (Takara Shuzo, Kyoto, Japan) for 30 cycles, with each cycle consisting of 94°C for 30 s, 62°C or 65°C for 30 s, and 72°C for 20 s, with an additional 10-min incubation at 72°C after completion of the last cycle.

Immunohistochemical and Immunocytochemical Analysis

Immunohistochemical analysis was performed as previously described (Mori *et al.*, 2005). Briefly, the sections were incubated for 1 h at room temperature with mouse mAb against vimentin (Cone V9, DakoCytomation, Fort Collins, CO). After washing in PBS, sections were incubated with horseradish peroxidase-conjugated rabbit anti-mouse immunoglobulin, diluted, and washed in cold PBS. Staining was developed by using a solution containing diaminobenzidine and 0.01% H₂O₂ in 0.05 M Tris-HCl buffer, pH 6.7. Slides were

counterstained with hematoxylin. In the cases of fluorescence, frozen sections fixed with 4% PFA were used. The antibodies against human dystrophin (NCL-DYS3; Novocastra, Newcastle upon Tyne, United Kingdom) or anti-human nuclei mouse mAb (clone 235-1, Chemicon, Temecula, CA) was used as a first antibody, and goat anti-mouse IgG conjugated with Alexa Fluor 488 or goat anti-mouse IgG antibody conjugated with Alexa Fluor 546 (Molecular Probes, Eugene, OR) was used as a second antibody.

Immunocytochemical analysis was performed as previously described (Mori *et al.*, 2005), with antibodies to skeletal myosin (Sigma, St. Louis, MO; product no. M 4276), MF20 (which reacts with all sarcomere myosin in striated muscles, Developmental Studies Hybridoma Bank, University of Iowa, IA), α -sarcomeric actin (Sigma, product no. A 7811), and desmin (BioScience Products, Bern, Switzerland; no. 010031, clone: D9) in PBS containing 1% bovine serum albumin. As a methodological control, the primary antibody was omitted. In the cases of fluorescence, slides were incubated with Alexa Fluor 546-conjugated goat anti-mouse IgG antibody.

Western Blotting

Western blot analysis was performed as previously described (Mori *et al.*, 2005). Blots were incubated with primary antibodies (desmin, myogenin [Clone F5D, Santa Cruz Biotechnology], and dystrophin [NCL-DYSA, Novocastra]) for 1–2 h at room temperature. After washing three times in the blocking buffer, blots were incubated for 30 min with a horseradish peroxidase-conjugated secondary antibody (0.04 μ g/ml) directed against the primary antibody. The blots were developed with enhanced chemiluminescence substrate according to the manufacturer's instructions.

Fusion Assay

EM-E6/E7/hTERT-2 cells (2500/cm²) or EGFP-labeled EM-E6/E7/hTERT-2 cells (2500/cm²) were cocultured with C2C12 myoblasts (2500/cm²) for 2 d in DMEM supplemented with 10% FBS and then cultured for 7 additional days in DMEM with 2% HS to promote myotube formation. The cultures were fixed in 4% paraformaldehyde and stained with a mouse anti-human nuclei IgG1 mAb and the mouse anti-human dystrophin IgG2a mAb (or anti-myosin heavy chain IgG2b mAb MF-20). The cells were visualized with appropriate Alexa-fluor-conjugated goat anti-mouse IgG1 and IgG2a (or IgG2b) secondary antibodies (Molecular Probes). Total cell nuclei were stained with DAPI (4',6-diamidino-2-phenylindole).

In Vivo Cell Implantation

Six- to 8-wk-old NOD/Shi-scid/IL-2 receptor $-/-$ (NOG, CREA, Shizuoka, Japan) mice and 6- to 8-wk-old mdx-scid mice were implanted with EM-E6/E7/hTERT-2 cells and menstrual blood-derived cells in seven independent experiments. The cells (2×10^7) were suspended in PBS in a total volume of 100 μ l and were directly injected into the right thigh muscle of NOG mice or mdx-scid mice. The mice were examined 3 wk after cell implantation, and the right thigh muscle was analyzed for human vimentin and dystrophin by immunohistochemistry. The antibodies to vimentin and dystrophin (NCL-DYS3) react with human vimentin and dystrophin-equivalent protein, but not murine protein.

RESULTS

Surface Marker Expression of Endometrium-derived Cells

We investigated myogenic differentiation of primary cells without gene introduction from menstrual blood, because menstrual blood on the first day of the period is considered to include endometrial tissue. We successfully cultured a large number of primary cells from menstrual blood. Menstrual blood-derived cells showed at least two morphologically different cell groups: small spindle-like cells and large stick-like cells, regarded as being passage day (PD) 1 or 2 (Figure 1, A and B, respectively). Surface markers of the menstrual blood-derived cells were evaluated by flow cytometric analysis. Surface markers of EM-E6/E7/hTERT-2 cells (Figure 1C) and menstrual blood-derived cells (Figure 1D) were evaluated by flow cytometric analysis (Figure 1E). In these experiments, the cells were cultured in the absence of any inductive stimuli. EM-E6/E7/hTERT-2 cells were positive for CD13, CD29 (integrin β 1), CD44 (Pgp-1/ly24), CD54, CD55, CD59, CD73, and CD90 (Thy-1), implying that EM-E6/E7/hTERT-2 cells expressed mesenchymal cell-related antigens in our experimental setting. Menstrual blood-derived cells were positive for CD13, CD29, CD44, CD54, CD55, CD59, CD73, CD90, and CD105, implying that prolif-